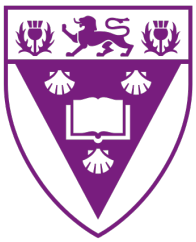

RHODES UNIVERSITY

Where leaders learn

The dispersion measure in broadband data from radio pulsars

Dissertation submitted in fulfilment of the

requirements for the degree of

MASTERS IN SCIENCE

in the Department of Physics and Electronics

RHODES UNIVERSITY

Author:

Isabella Rammala

Supervisors:

Prof. Aris Karastergiou

Dr. Griffin Foster

Prof. Oleg Smirnov

February 2018

Abstract

Modern day radio telescopes make use of wideband receivers to take advantage of the broadband nature of the radio pulsar emission. We ask how does the use of such broadband pulsar data affect the measured pulsar dispersion measure (DM). Previous works have shown that, although the exact pulsar radio emission processes are not well understood, observations reveal evidence of possible frequency dependence on the emission altitudes in the pulsar magnetosphere, a phenomenon known as the radius-to-frequency mapping (RFM). This frequency dependence due to RFM can be embedded in the dispersive delay of the pulse profiles, normally interpreted as an interstellar effect (DM). Thus we interpret this intrinsic effect as an additional component δDM to the interstellar DM, and investigate how it can be statistically attributed to intrinsic profile evolution, as well as profile scattering. We make use of Monte-Carlo simulations of beam models to simulate realistic pulsar beams of various geometry, from which we generate intrinsic profiles at various frequency bands. The results show that the excess DM due to intrinsic profile evolution is more pronounced at high frequencies, whereas scattering dominates the excess DM at low frequency. The implications of these results are presented with relation to broadband pulsar timing.

Contents

List of Figures

List of Tables

Acknowledgements

I would like to thank my primary supervisor, Aris Karastergiou, for proposing and allowing me to work through this project. I would like to commend him for his constant encouragement, patience and willingness to take time and explain even the simplest concepts to me. His positive guidance throughout this research will always be cherished. I would also like to thank my secondary supervisor, Griffin Foster, for always be willing to answer my questions regarding python programming and for providing useful comments during the preparation of this thesis.

I would also like to thank the pulsar team at the Square Kilometre Array South Africa (SKA SA) for their constant support throughout the duration of my research years; Maciej Serylak for always having an open door when I need a quick explanation on certain concept, Marisa Geyer for providing her scattering routine used in a section of our analysis. I would also like to send my gratitude to Monica Obrocka for the writing and coding tips, as well as my manager Sharmila Goedhart for allowing me time to dedicate to the preparation of this thesis. My gratitude also goes to my family for their constant encouragement. And finally, I would like acknowledge the SKA SA for the financial assistance.

Chapter 1

Introduction

Radio pulsars are characterized as dense, fast rotating and highly magnetised neutron stars, they are remnants of stars that are not massive enough to become black holes but too massive to become white dwarfs.

It has been proven for a majority of pulsars that a pulsar is a neutron star formed when a massive star runs out of fuel and core-collapses under its own gravity through a supernova explosion. During the core collapse, the conservation laws take effect. Angular momentum is conserved, leading to increased strong surface magnetic field and to a rapid increase of the rotational velocity of the remaining compact object - pulsars have rotation periods of a few seconds down to milliseconds (where they are called millisecond pulsars or MSPs). As they age, they lose their rotation power and spin down to longer rotational periods [Lorimer and Kramer, 2005].

There are currently over 2500 known pulsars [1], many of which are known

[1] All confirmed known pulsars are constantly updated in the ATNF catalogue, accessed at `https://www.atnf.csiro.au/research/pulsar/psrcat/` [Manchester et al., 2005].

to exist as isolated objects, while some are in binary systems and even in a triple stellar system e.g. PSR J0337+1715, a MSP with two white dwarfs [Ransom et al., 2014] or PSR B1620-26, a possible triple system consisting of a pulsar, white dwarf and a planet [Thorsett et al., 1993][2].

Although pulsars were first discovered in the radio region of the electromagnetic spectrum [Hewish et al., 1969], some pulsars have also been observed at gamma ray wavelengths, X-rays and even at optical wavelengths. The study of pulsars at radio wavelengths, however, provides information about the pulsar magnetosphere, the polarization properties of the radio emission, and improves our understanding of how pulsar radiation interact with the interstellar medium (ISM).

One of the major radio pulsar projects that involve the use of pulsars as tools is "pulsar timing", which is the regular monitoring of the time of arrival (TOA) of the pulses from a pulsar. When many pulsars are timed with high precision (the so-called pulsar timing array (PTA)), a correlated signature in their TOAs can be associated with an external effect such as a gravitational wave passing through the line of sight towards these sources [Manchester, 2010]. The International Pulsar Timing Array (IPTA) is a collaboration of international PTA associations with a common goal of using pulsars as tools to detect gravitational waves [3]. Each of these PTA associations has telescopes that observe the selected pulsars at various frequency band, all of which have broadband receivers (see discussions in section 1.2). It is important for this

[2]See also, for example, this interactive programme that plots the currently known pulsars in the galaxy (`http://www.ishivvers.com/maps/pulsars.html/`).

[3]The IPTA currently consist of the European Timing Array (EPTA), the North American Nanohertz Observatory for Gravitational Waves (NANOGrav), and the Parkes Pulsar Timing Array (PPTA). See the IPTA website `http://www.ipta4gw.org/`

common goal that the pulse TOAs from the PTA pulsars are measure with high precision.

High precision pulsar timing relies on precise measurements of the pulse profiles, and an assumption that the profiles do not change on long timescales. It is therefore essential that we understand the behaviour of these pulse profiles, how they are emitted, how can they be affected by physical processes intrinsic to the pulsar, the ISM and even by how we measure them with our telescopes.

Future plans for pulsar surveys are to build telescopes with broadband receivers. Such telescopes promise to increase the sensitivity with which observations will be performed and in turn improve timing precision. In this study, we will investigate how the use of such broadband pulsar data may introduce errors to the determination of pulsar dispersion measure (to be explained in detail in the following sections), which is one of the important parameter in high precision timing.

In order to perform our experiments, we require some background information about how pulsars emit radio waves and the relationship with the observing frequencies. The following sections will thus discuss some of the pulsar observables, from which the theoretical models of pulsar beams that are important for our investigations, are derived.

1.1 Observational aspects of pulsars

It is now accepted that radio emission from pulsars is emitted in the pulsar magnetic poles (Figure 1.1). The neutron star acts as a giant magnet, sur-

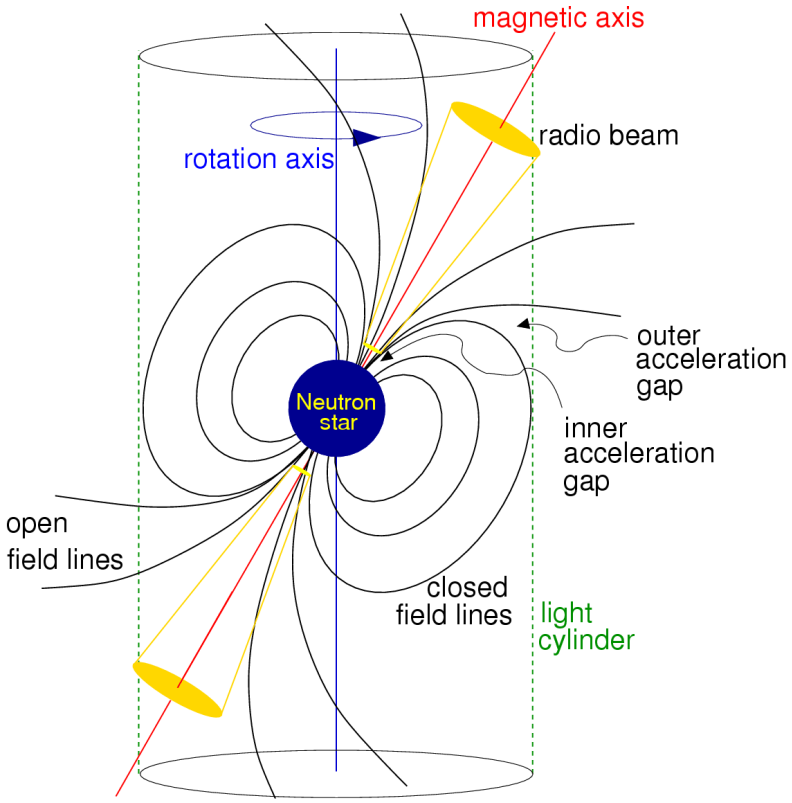

Figure 1.1: A toy-model used to explain the origin of the pulsed emission from pulsars is called the lighthouse model. In this model, the radio emission is beamed from the magnetic poles. This beam is inclined from the pulsar rotation axis and a pulse-like emission is detected every time the beam sweeps through an observer's line of sight (figure adopted from Lorimer and Kramer [2005]).

rounded by magnetic fields in co-rotation. At some distance from the surface of the neutron star (a limit called the light cylinder in figure 1.1), the plasma in the magnetic poles reaches the speed of light; here the field lines are open and radio emission is beamed [Lorimer and Kramer, 2005].

This beam of radiation is inclined with respect to the rotation axis at some angle due to the misalignment of the magnetic axis and spin axis. The "pulsed" nature of the emission is a due to the rotation of the pulsar relative to the detector. A pulse-like emission is observed with every rotation as the beam sweeps in and out of the observer's line of sight (LOS), analogous to a lighthouse beam.

Individual pulses from each rotation have been observed to be very different, owing to dynamic processes in the pulsar magnetosphere (a plasma-filled region above the neutron star surface). However, when averaged together, the resultant profile is in general very stable (Figure. 1.2) for a given pulsar, but quite different from source to source, and depends on how the LOS cuts the beam (see Subsection 1.1.2 for a detailed description). Pulsar timing, is dependent mostly on the study of these average profiles.

Radio pulsars are very weak radio sources and most of the signal can be buried in noise. Hence, to improve the signal-to-noise ratio, large telescopes are used. In addition, receivers can be built in such a way that they can observe across a wide pre-determined frequency band to take advantage of the pulsar broadband nature. These broadband data are channelised and, after integration, each channel contains an average of the accumulated single profiles at a given frequency. The channelised profiles are averaged across multiple epochs to obtain a stable average profile, and thus long integration

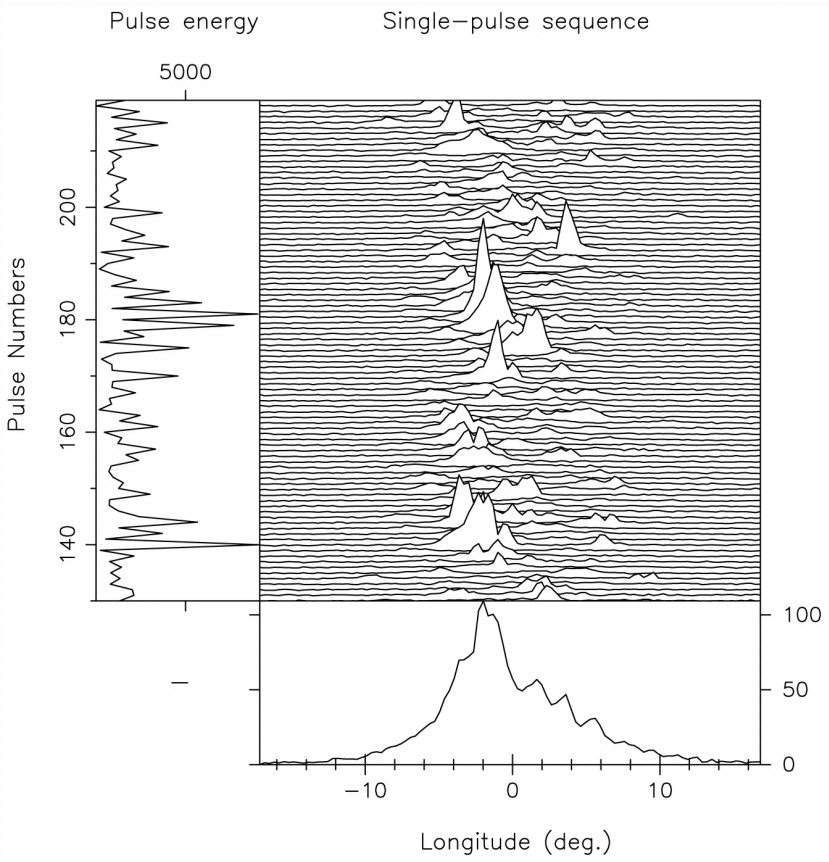

Figure 1.2: A sequence of individual pulses from every rotation for pulsar PSR B0943+10 on the center panel (adopted from Deshpande and Rankin [1999]). The left panel shows the energy of the individual pulses, which can vary dramatically. When averaged together, an average profile is obtained (bottom panel). Such an average profile tends to be relatively stable.

time contribute to improve the S/N.

Despite the fact that an average profile is stable at a given frequency, the pulse profile evolves with frequency. The width of the profile in most cases tends to increase with decreasing frequency and if the profile has multiple components, the component separation also increases with decreasing frequency (see for example Karuppusamy et al. [2011]). Above 1 GHz, however there is typically no significant narrowing of the pulse profile. Such behaviour is explained by the radius-to-frequency mapping model which is presented in detail in the following subsection.

1.1.1 Radius-to-frequency mapping

As already mentioned in Section 1.1, pulsar radio emission is understood to come from a plasma-filled magnetosphere. The exact process that produces this radiation is not well understood, and is currently a topic of active research. For the sake of our study, and for simplicity, we adopt the the Goldreich and Julian [1969] model of the pulsar magnetosphere electrodynamics. We think of a pulsar as rotating spherical magnet because of their strong magnetic fields. Upon rotation, the magnetic fields induce electric fields. The resultant Lorentz forces pull charges from the surface in the magnetic poles. This creates the co-rotating, plasma-filled, magnetosphere where charges moves along the magnetic field lines, and are emitted as radio waves.

Although the nature of a pulsar magnetosphere is not well understood, observed phenomenologies have been used to infer the proposed models of the magnetosphere, three of which are discussed in details later in the section that follows (Section 1.1.2).

An example of such an observed phenomenon is the evolution of pulse profiles with observing frequency. PSR B1133+16 is an example of a pulsar that clearly exhibits profile evolution. The profile of this pulsar is made up of two components that tend to narrow and move closer to each other at increasing frequency, from $<$ 100MHz up to $>$ 1GHz [Thorsett, 1991]. This intrinsic frequency dependent evolution is separate from the observed broadening due to propagation through the interstellar medium [Cordes et al., 2016].

The phenomenon of intrinsic profile evolution with frequency is naturally explained by Cordes [1978] as the result of high frequencies being emitted at smaller radius (or height above the neutron star surface) and lower frequencies at larger radius. If we consider again the Goldreich and Julian [1969] model, we would expected large particle densities closer to the surface and fewer at higher altitudes; consequently, we expect higher plasma frequencies at lower altitudes. If we consider also the curved nature of the magnetic field lines, together with the height dependent frequencies, the higher frequencies are emitted at smaller beam opening angles and the lower frequencies at larger beam opening angles. This is commonly referred to as radius-to-frequency mapping (RFM), and relates the emission altitude with observing frequency. Thus in the RFM model, high frequencies are emitted at lower altitudes and lower frequencies higher up in the magnetosphere.

Streams of particles in the dipolar magnetic field co-rotate with the pulsar up to a distance away from the neutron star surface where the particles reach the speed of light. This distance is commonly referred to as the light cylinder radius (see Figure 1.1). Magnetic field lines that do not close within the light cylinder radius give rise to particle acceleration and consequently radio

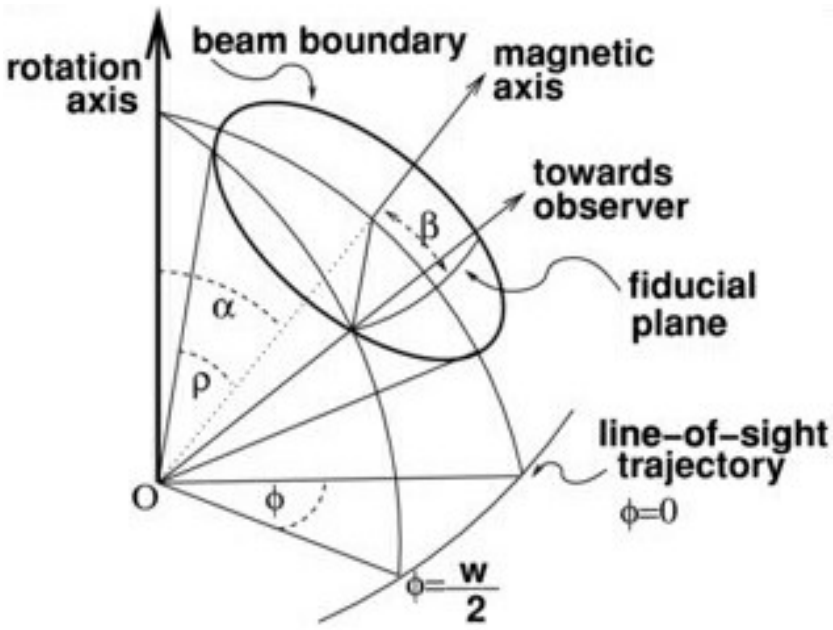

Figure 1.3: A general beam geometry of a pulsar's magnetosphere where radio emission is beamed. The open field lines form a cone-like beam centered around the magnetic axis. The magnetic axis is inclined from the rotation axis with an angle α. The size of the beam is given by the opening angle ρ. As the pulsar rotates, an observer's line of sight reaches a minimum angular distance from the magnetic axis, at the impact parameter β. The rotation phase is represented by the angle ϕ.

emission. The radio beam is bound by the last open field lines, and has a particular opening angle ρ centred onto the magnetic axis at every height from the surface of the pulsar. This opening angle ρ is defined in radians by Lorimer and Kramer [2005]

$$\rho \approx \sqrt{\frac{9\pi H_\nu}{2cP}}, \tag{1.1}$$

where c is the speed of light, P is the period of rotation, and H_ν is the frequency dependent emission altitude defined below.

In a generally accepted picture of the beam geometry (Figure. 1.3), the magnetic axis is inclined with angle α relative to the spin axis. As the pulsar rotates through a rotation phase ϕ, the beam sweeps an observer's line of sight, reaching a minimum angular distance from the magnetic axis of β, also known as the impact parameter.

Thorsett [1991] derive the frequency relation with emission altitude as a broken power law

$$H_\nu = K\nu^q + C, \tag{1.2}$$

where H_ν is the frequency dependent emission altitude and C a constant that ensures little to no evolution at frequencies above 1 GHz. The RFM index q has been determined for different pulsars in Thorsett [1991] and Hassall et al. [2012] among others.

Taking this geometry as the accepted general pulsar beam geometry, some observational models have been introduced to explain the possible shape of the beam, given the observed pulsar profiles.

1.1.2 Pulsar beam models

Hollow cone beam

The hollow cone beam model [Backer, 1976] is one of the first proposed models, in an attempt to explain the variety of observed pulse profile shapes from radio pulsars (Figure 1.4). The hollow cone beam model suggests that emission comes from a single hollow cone of emission with a co-axial core. The observed profile complexity comes from different line of sight cuts through the cone beam. The model has difficulties producing many observables for pulsar

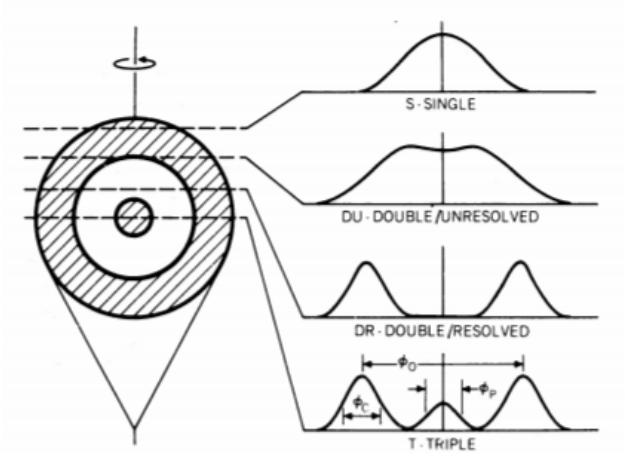

Figure 1.4: A cartoon showing the Backer [1976] hollow cone beam model and profiles depending on how an observer cuts the beam (figure adopted form Rankin [1983]).

profiles. For example, this model cannot reproduce profiles with complex components. The model also relies on some form of RFM to explain profile evolution with frequency which is observed for many profiles across wide frequency bands.

This model was later advanced by Rankin [1983] where she introduced nested hollow cones responsible for what they refer to as conal emission and a quasi-axial core of emission. Rankin [1983] suggest that conal and core emission arise from different altitudes above the neutron star surface, with core emission originating from lower altitudes and conal emission from higher altitudes. Due to the diverging nature of the magnetic field lines, when the cones are projected onto the observer's plane, cones emitted at lower altitudes appear smaller compared to cones emitted at higher altitudes. Thus the widths of profiles observed at low frequencies are wider than profiles at high frequencies.

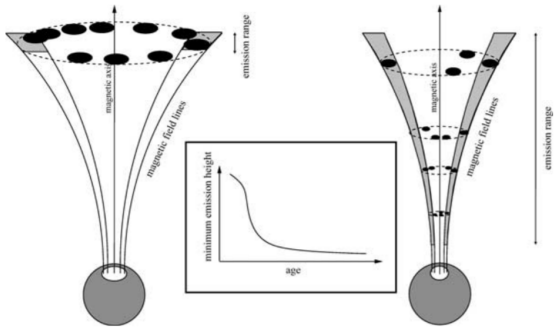

Figure 1.5: A cartoon showing a conal-patcy beam model for a young pulsar (left) and old pulsars (right). The beam of this model is patchy with emitting regions at discrete emission heights. In this model, young pulsar have small emission range at higher altitudes above the neutron star surface, and wide range of emission heights that extends closer to the surface (cartoon from Karastergiou and Johnston [2007]).

Conal-patchy beam

Lyne and Manchester [1988] propose that, unlike the nested cones in Rankin [1983], the emission beam consists of discrete emission regions within the opening radius of the polar cap. However, Lyne and Manchester [1988] do not discuss the origin of radius to frequency mapping. Karastergiou and Johnston [2007] proposed a conal-patchy beam model where emission comes from a set of curved open dipolar magnetic field lines confined by the last open field lines within the polar cap. Specifically to this model, the pulsar beam is populated with discrete emitting regions at multiple distinct altitudes along the field lines. The authors use this model to explain the observed variety of average pulse profiles for young and old pulsars. For this model, pulsars with spin period below 0.15 s are regarded as young pulsars and pulsars with spin period above 0.15 s as old pulsars. Generally, young pulsars have simple profiles (single or double component [Johnston and Weisberg, 2006]) whereas old pulsars profiles appear to have complex components e.g. PSR B0329+54

which has approximately nine components [Gangadhara, 2000].

In terms of RFM, this model suggests that the distinct height at which each emitting region occurs is frequency dependant in the typical sense. For example, if for some pulsar the radio emission arises from heights A, B, C at some frequency, then at a lower frequency the emission is suggested to arise from higher heights A', B', C', with A'>A, B'>B, C'>C.

In order to take into account the differences in young and old pulse profiles shapes, the model in Karastergiou and Johnston [2007] can be a wide beam with a small range of emission altitudes higher in the magnetosphere for young pulsars, which can explain the origin of simple, wide profiles. Conversely, the model can also produce beams where emission altitudes extend from higher in the magnetosphere, down towards the neutron star surface. Complex profiles like those of older pulsars can come from the line of sight intersecting the same field lines at multiple discrete heights. This model was, however, only developed based on the observational behaviour of normal young and old pulsars and suffers to explain profiles for millisecond pulsars. Moreover, the model lacks a theoretical basis.

Fan beam

The stream model or fan beam model was first introduced by Michel [1987]. In this model, emission regions extend along a set of curved azimuthal magnetic field lines that form a fan-like beam. Particles stream along the field lines, causing fully illuminated magnetic field lines that act as flux tubes where radiation is emitted. Recently, in Wang et al. [2014], Dyks and Pierbattista [2015], and Dyks and Rudak [2015] it was shown that this model

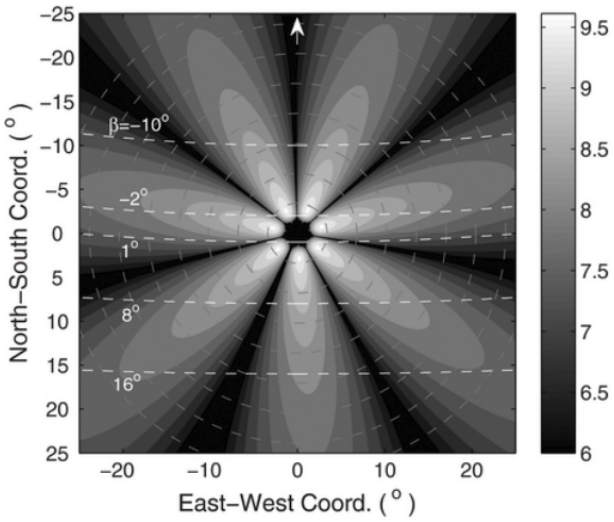

Figure 1.6: A fan beam model simulation from Wang et al. [2014]. The beam is illuminated with "flux tubes" of emission along the field lines. The high frequency flux tubes are indicated buy the bright areas closer to the magnetic poles (0,0). The low frequencies are represented by wide grey areas further from the pole.

is consistent with some observational phenomena. Saha and Dyks [2017] explains the pulse profile evolution of PSR J0737-3039B (the 2.8s pulsar in the famous double pulsar binary system) as due to the beam of this pulsar consisting of elongated patchy emission regions, orientated in a longitudinal direction along the field lines. This work also introduces the possibility of multiple fan-like sub-beams which can take different orientations in order to explain different pulse profile behaviour (see Saha and Dyks [2017, figure 9]).

The origin of RFM in the fan-beam model is explained in Dyks and Rudak [2015] where the streams, or flux tubes along the flaring dipole field lines are projected onto the plane of the sky to create two-dimensional gaussian patterns (e.g Figure 1.6). Similar to the classical hollow cone model, emission arises at one altitude per frequency, but the emission patch extends across a

large height range as a function of frequency. The curved nature of the field lines causes the flux tubes to form sub-beams whose widths increase with increasing radius, explaining the origin of profile widening with decreasing frequency [Dyks and Pierbattista, 2015]. This also may result in a frequency dependent shift of the center of the peak relative to the dipole axis along the curved field line.

1.1.3 Interstellar effects

Dispersive delays

The intrinsic pulsar radiation emitted from the pulsar beam in the magnetosphere (whichever model is used) traverses the interstellar medium (ISM). During propagation, the waveform interacts with the free electrons in this cold, magneto-ionised plasma. This interaction leads to a frequency dependent group velocity delay of the waveform, which is exaggerated at low frequencies. Thus, when observed at some frequency band, the low frequency pulse profiles are delayed in phase with respect to the high frequency profiles. The interstellar dispersive time delay (in seconds) between two observing frequencies (ν_1 and ν_2 in MHz) is given by

$$\Delta t = 4.15 \times 10^3 \mathrm{s} \left(\nu_2^{-2} - \nu_1^{-2}\right) \int_0^d n_e dl \tag{1.3}$$

where $DM = \int_0^d n_e dl$ (known as the dispersion measure) represents the average electron (n_e) column density in the observer's line of sight to a pulsar at some distance (d). In pulsar observations, the dispersive delay across a given frequency band results in a characteristic quadratic curve, with the higher

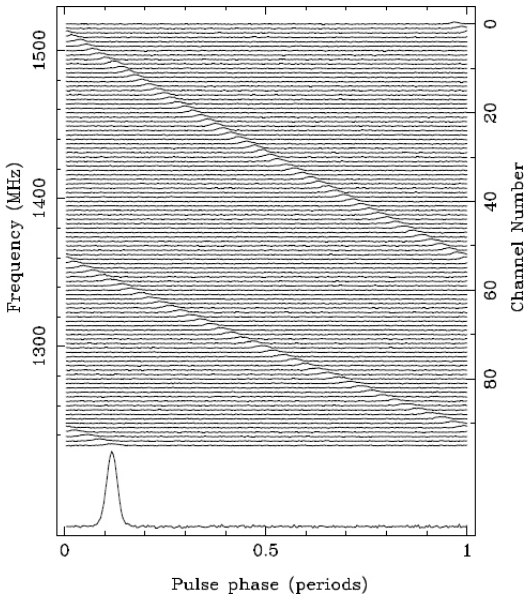

Figure 1.7: An example of pulsar dispersion across a frequency band from the Parkes telescope. The plot shows an observation of the 128 ms pulsar PSR B1356-60 with a DM of 295 $\mathrm{pc\,cm^{-3}}$ [Lorimer and Kramer, 2005]. The top panel shows a quadratic sweep of the profile, displaying the delay at low frequency relative to high frequency profile. The bottom panel shows an average profile with the dispersion correction (de-dispersion).

frequencies arriving at earlier times and the lower frequencies at later times.

Figure 1.7 shows an example of a pulsar observation in a given frequency band. There is a quadratic profile shift across the band (top panel) that wraps at the bottom of frequency from profile averaging. The average profile (after de-dispersion) is shown at the bottom of the profile. Without dispersion correction, the average profile would be a wide, low signal-to-noise profile. This illustrates why it is important to obtain a correct DM for pulsar studies in the profile domain.

Scattering

Another effect of the ISM that can change the relative pulse phase associated with the peak of the profile at different frequencies, is scattering. Inhomogeneities in the electron densities of the ISM, in other words electron density gradients Δn_e, lead to frequency dependent diffractive and/or refractive scattering of the emitted radio waves. This scattering causes multi-path propagation of the radio waves, such that the observed average pulse profile carries the signature of these ISM delays.

Assuming the simple case of the ISM being a single, thin scattering screen between the observer and the pulsar, as described in e.g. Williamson [1972], the scattering imprint is mathematically characterized by the convolution of the pulse shape with an exponential function $e^{-\Delta t/\tau_s}$, where Δt is the time delay (in seconds) due to the multi-path propagation and $\tau_s \propto \nu^{-4}$ is the scattering time scale (in seconds).

Bhat et al. [2004] derives the empirical relationship between the scattering time scale (τ_s) and the DM as

$$\log(\tau_s) = -6.46 + 0.154\log(DM) + 1.07(\log DM)^2 - 3.86\log(\nu) \qquad (1.4)$$

where ν is the observing frequency in GHz, DM the interstellar dispersion measure in $\mathrm{pc\,cm^{-3}}$ and τ_s the scattering time scale in ms. Thus the ν^{-4} scale implies that profiles at large distances (or profiles with large DM) will experience large scattering at low frequencies. In addition, the low frequency profiles experience high scattering compared to profiles at high frequencies. Thus at low frequencies, scattering effect cause profile to exhibit relative

peak phase shifts. Moreover, due to relative motions of the Earth, the solar system, and the pulsar, the line-of-sight changes, and radiation from the pulsar propagate different regions of the ISM. Thus what is observed is a time variable DM [Cordes et al., 2016].

The above mentioned phenomena have a frequency dependence. It is therefore worth investigating how introducing the use of broadband data will affect our measurable, namely the DM which inferred by measuring how much profiles are delayed across the band.

1.2 Broadband pulsar astronomy

Although exact nature of the radio pulsar emission remains unknown (Jones [2017], Melrose [2017], etc.), there is an observed dependence of the radio properties of the pulsar population on the frequency and bandwidth used. The frequency dependence of any observable quantity, such as pulse width and shape, flux density, and polarization can be used as a diagnostic in understanding the physical processes at play. These physical processes can be intrinsic to the pulsar and its immediate environment, as well as related to propagation of the radiation through interstellar space.

New receivers attached to large radio-telescopes today allow for simultaneous observation of broad frequency bands, in order to take advantage of the broadband nature of pulsars to increase the observed signal-to-noise ratio (S/N). These receivers provide the opportunity to observe the emission process continuously with frequency, as opposed to the narrow bands that have been employed historically. This requires some consideration for profile

domain pulsar astronomy where profiles have been observed to evolve with frequency (e.g Thorsett [1991]).

The common property that the models in Section 1.1.2 adopt is some form of RFM, which relates the observed profile width at a given observing frequency with the height of emission [Cordes, 1978]. The interpretation is therefore that the wide, low frequency profiles [Bilous et al., 2014] are emitted at higher altitudes, and that the narrow, high frequency profiles are emitted at lower altitudes. In general, this profile evolution with frequency results in particular features of the pulse profile being observed at different pulse phase at different frequencies. However, the magnitude of the effect will depend on the exact profile evolution within a given frequency band.

From the previous sections it is also clear that observed pulse profiles contain an imprint of the processes that operate at the neutron star and in the ISM. A broadband observation of a pulse profile from a known pulsar, will show the effects of dispersion, scattering and intrinsic beam evolution with frequency. Traditionally, these three effects are treated separately. Dispersion measures are determined by maximizing the peak S/N of a "de-dispersed" profile that has been integrated in frequency. Scattering is measured by either deconvolution or forward modelling of scatter-broadened profiles (scintillation measurements are performed on dynamic spectra rather than pulse profile data), assuming specific laws for the behaviour of the ISM. Intrinsic profile evolution has also historically been measured independently of the ISM effects Thorsett [1991], with some recent notable exceptions [Hassall et al., 2012].

Pulsar timing can also benefit from the use of broadband observations.

This is because the simultaneous multi-channel observation means a significant number of pulses will be averaged, which translates into a high S/N. The high S/N profile implies a better accuracy in choosing a point in the pulse profile to use as a reference point to measure TOAs - the easiest way is to select the phase peak of the profile as the reference.

The traditional method used for pulsar timing involves correcting for ISM dispersive delays by de-dispersing the profiles with a DM predetermined during pulsar searching surveys at any observing frequency, depending on the telescope used. The profiles are then averaged together across all the frequency channels in the band to obtain a stable profile that can be cross-correlated with a template to determine the pulse TOA. This method is known as the template-matching method [Lorimer and Kramer, 2005].

A template is mainly obtained from adding many observations of the same pulsar. In general, a profile $P(t)$ cross-correlated with this template $T(t)$ is assumed to be a scaled version of template, delayed by time ($\Delta\tau$) with added noise $N(t)$

$$P(t) = a + bT(t - \Delta\tau) + N(t) \tag{1.5}$$

where a is the offset and b is the scaling factor. This traditional method becomes a problem when using broadband data where profiles vary with frequency.

Liu et al. [2014] presents a more sophisticated two-dimensional equivalent of the template-matching method for broadband pulsar timing data analysis, which corrects for the frequency and time dependent effects in the template, but requires a template in each channel of the observing band. The problem

that rise with this method, and all other template-matching methods, is the determination of a reference point on the profile which can be easily identified and tracked across all profiles in the band to determine relative delays.

This reference point, commonly referred to as the "fiducial point", can be thought of as an imaginary flag on the pulsar (and consequently on the pulse profile), such that one can identify the position of this flag on the profile at any given moment for each rotation. When such a point can be easily and accurately identified on the profiles, and the template, the pulse TOA can be accurately identified through cross-correlation.

Traditionally, the profile peak is selected as a fiducial point for profiles at any frequency. Selecting the profile peak as a fiducial point poses problems as well. Firstly, for wider profiles, a fiducial point selected this way will have large uncertainty as it is difficult to identify where the profile peaks. Secondly, the frequency dependent profile evolution can introduce errors in pulsar timing and TOA measurements when using broadband data. Across a wide frequency band, profile evolution can move the fiducial point of the average profile, which also affect the S/N of the frequency-integrated profile. This becomes even more problematic, especially when variations of DM are not accounted for.

Ahuja et al. [2007] have studied the variations of DM for PSR B1642-03 and PSR B0329+54 between 240 MHz and 610 MHz where they find that larger DMs are measured when determined at higher frequency. They identify one possible cause of such a discrepancy as the result of the pulsar beam geometry; more specifically, the assumption of the RFM in pulsar magnetosphere which may result in the low frequency radiation sweeping

the line of sight earlier than the high frequency radiation, right before they interaction with the ISM, which has an opposite effect.

Following these findings, the question we ask in this thesis is, how much of the pulsar DM component can be statistically attributed to beam and profile evolution with frequency due to the frequency dependent height of emission. To investigate this we make use of the beam models discussed above to simulate pulsar profiles across wide frequency bands, typical current broadband telescopes. We also include scattering effects, which can contribute and additional component to the measured DM.

The chapters that follow will present the procedures followed for the investigations. In Chapter 2 we present the code written to simulate the pulsar beams and profiles. This forms a large part of our investigation since we want to produce more realistic profiles which include possible frequency dependent behaviour of the emission from the pulsar magnetosphere. Chapter 3 presents the procedure used to generate a Monte-Carlo experiment of many pulsar simulations at various bands. The results from these experiments are presented in Chapter 4. In Chapter 5 we discuss the implications of the simulation results and conclude our investigation in Chapter 6.

Chapter 2

Simulation code

The exact nature of the pulsar beam and processes that produce radiation are not well understood (Section 1.1). However, we can make use of observational phenomena as well as statistical simulations to infer the possible radio emission processes. The following sections give a description of some of the important functions of the simulation code used to generate pulsar beams and resultant pulse profiles which we use to search for the additional, profile-specific component to the measured DM.

Section 2.1 constitutes an extended `python` version of the work by Karastergiou and Johnston [2007] which was initially written in `fortran`, with the aim to produce a general pulsar observed beam model that explains the observational phenomena of both young and old pulsar profiles. We expand the code to simulate profiles with option to chose additional pulsar beam models discussed in Sub-section 1.1.2. Moreover, a subset of the routines in Section 2.2 are also a collaborative work that follow the techniques in Geyer et al. [2017] used to fit scattering in low frequency pulsar profiles.

2.1 Intrinsic profiles

Radio pulsar beam models predict (amongst other phenomena) that radiation is beamed at some height above the surface of the star in the magnetosphere (Backer [1976], Rankin [1983], Karastergiou and Johnston [2007]).The frequency of emission appears to be related to some height above the pulsar surface in the magnetosphere, the so-called radius-to-frequency mapping model or RFM (see Section 1.1.1). The RFM model provides an equation that allows us to determine the heights at which radio pulsars emit, given the observing frequencies (Equation 1.2).

The following code determines these heights of emission, given the rotation period, the number of height components as proposed by Karastergiou and Johnston [2007], as well as minimum and maximum possible emission heights. An option in the code is to use additional models for the simulation (hollow cone beam model [Backer, 1976] or fanbeam model [Michel, 1987] - the conal-patchy beam model [Karastergiou and Johnston, 2007] is adopted as the default model for the simulation).

```
1  def emission_height(P, ncomp, iseed, hmin,
2      hmax, fanBeam=None, hollowCone=None):
3      """
4      Function to determine emission heights
5      given the spin period. If no emission height
6      range is specified, the default used for P < 0.15 s
7      is between [950, 1000] km and between [20, 1000] km
8      for P > 0.15 s as in KJ07.
9      Args:
10     ----
```

```
    P       : rotation period (seconds).
    ncomp   : integer number of components.
    iseed   : integer seed for random generator.
    hmim    : minimum possible emission heights (km).
    hman    : maximum possible emission heights (km).
    freq    : observing frequency (GHz)

    Return:
    _______
    H       : The possible heights (km) given period P (s).
    """
    np.random.seed(iseed)
    if fanBeam or hollowCone:
       num_H = 1
    else:
        num_H = ncomp # number of discrete emission heights
    # If height range is not specified:
    if hmin == None and hmax == None:
        # emission height for a short period pulsar
        if P <= 0.15:
            hmin = 950
            hmax = 1000
            H = np.random.uniform(hmin, hmax, size=1)
        elif P > 0.15:
            hmin = 20
            hmax = 500
            H = np.random.uniform(hmin, hmax, size=num_H)
    # For specified height range:
    else: H = np.random.uniform(hmin, hmax, size=num_H)
    # Scale the height with frequency
```

```
41        gamma = 0.95
42        H_mu = H * (9 * freq**(-gamma) + 41)/float(9 + 41)
43        return H_mu
44
```

Listing 2.1: A function to determine possible emission height range give a pulse period. The function uses the emission height equation to predict the frequency dependent heights of emission, given the observing frequency.

The `emission_height()` function (Listing 2.1) determines the initial possible emission heights for a pulsar with a given rotation period P (Equation 1.2). If the hollow cone or the fan beam model is selected, the function will produce a single height of emission for a given frequency. This is expected from the hollow cone beam model where an emission ring comes from a single height at a given observing frequency. The possible height range is determined by the rotation period of the pulsar, as discussed by Karastergiou and Johnston [2007]. Observationally young, short period pulsars have a smaller range of emission heights, higher up in the magnetosphere, while larger emission height ranges are possible for the slower, older pulsars. To introduce the frequency dependence of the heights, we scale the height H using the frequency-dependent Equation (1.2), such that the emission heights are within the range specified by Karastergiou and Johnston [2007].

The size of the beam, also known as the opening angle ρ, is determined by the emission height and the rotation period (Equation 1.1). The equations estimate the size of the beam that is potentially observable at a given frequency. Function `rho()` (Listing 2.2) inputs the pulsar period in seconds as well as the emission height in kilometres and returns the opening angle in

degrees.

```
def rho(P, heights):
    """
    Function to determine the opening angle of the beam
    given the rotational period and emission height.
    Args:
    -----
    P          : Rotational period (seconds).
    heights    : Emission heights (km).
    Returns:
    --------
    rho        : The opening angle (degrees).
    """
    # Opening angle (eqn 3.29, Lorimer and Kramer 2005)
    numerator = np.sqrt((9 * np.pi * heights)
    denominator = (2 * (constants.c / 1000) * P)
    rho = np.rad2deg(numerator / denominator)
    return rho

```

Listing 2.2: The opening angle of the beam observable at a given frequency/height.

The center and width of the emitting regions within the beam can be estimated from the pulsar period and emission height. Assuming a patchy emission regions (within the beam) of size

$$w_p = 2.45^{\circ}\Delta s\sqrt{\frac{H_\nu}{10P}}, \tag{2.1}$$

as in Karastergiou and Johnston [2007], where Δs is 20% of the total available width [Johnston and Weisberg, 2006], H_ν the frequency dependent emission

height in Equation 1.2, and P the rotation period of the pulsar, Equation 2.1 can be used to determine the width of the discrete emitting regions for the Karastergiou and Johnston [2007] model (Listing 2.3). For the hollow cone beam model, the function `patch_width()` assumes the conal ring of emission is formed by many of these patches, distributed in a circular pattern along the field lines that form the beam. When many patches are distributed in a circular pattern to form a ring or emission required by the beam model, the model produces mainly unresolved double components or single components profile. Thus, to ensure that the hollow cone model also produces double-resolved components, patches whose size are a small fraction of the conal-patchy beam model are used.

```
1  def patch_width(P, heights, hollowCone=None):
2    """
3    Function to calculate the width of a patchy emission region
4    within a pulsar beam at a given height.
5    Args:
6    -----
7    P             : rotational period (seconds).
8    heights       : emission heights (km).
9    Returns:
10   --------
11   patchwidths   : the width of the patchy emission region
12                   (degrees).
13   """
14   #   width of the patch (eqn 3, KJ07):
15   if hollowCone:
16       # Smaller patches for the hollow cone (2.45 smaller
17       # than KJ07)
```

```
18          patchwidths = 0.2 * np.sqrt(heights / ( 10 * P))
19      else:
20          patchwidths = 2.45 * 0.2 * np.sqrt(heights / ( 10 * P))
21      return patchwidths
22
```

Listing 2.3: The width of the discrete emission regions within the beam.

The `patch_center()` function (Listing 2.4) also uses the period and the height of emission to map the azimuthal angle of the emission patches onto an observer's xy-plane, as the pulsar beam rotates. The function returns the x-y coordinates of the patches. For the hollow cone we produce arbitrarily, many patches with the same width, enough to form a conal ring at a given frequency. For the fan beam model, the same number of patches are arranged along the same azimuth such that they form a flux tube of emission at multiple heights/frequencies as required by the model, with the width depending on the height/frequency.

```
1   def patch_center(P, heights, npatch, iseed, fanBeam=None,
2                    hollowCone=None):
3       """
4       Function find centres of the patches
5       Args:
6       -----
7       P        : rotational period.
8       heights  : emission heights (in km).
9       npatch   : number of patches.
10      iseed    : random nunber seed.
11      fanBeam  : option to use fan beam model.
12
13      Returns:
```

```
14          ________
15          centerx : the patch center projection on the x-axis
16          centery : the patch center projection on the y-axis
17          """
18      # Find opening angle (size of the beam):
19      opa = rho(P, heights)
20      # Initialize parameters
21      centerx = []
22      centery = []
23      np.random.seed(iseed)
24
25      if hollowCone:
26          # For the hollow cone beam model:
27          # An arbitrary number of patches enough to fill circular
28          # ring
29          npatch = 40
30          # Azimuthal range of the position centers (degrees)
31          theta = 2 *np.arange(0, 2*np.pi, 2*np.pi/npatch)
32      elif fanBeam:
33          # For the fan beam model:
34          # Patches along the same azimuth to form a flux tube
35          theta = 2 * np.pi * np.random.random(npatch)
36      else:
37          # For the patchy beam model (default)
38          # Azimuthal positions for each component
39          theta = 2 * np.pi * np.random.random(len(heights)
40                  * npatch)
41      # Find the corresponding x-y coordinates
42      # for each emission height (comp!)
43      for j in range(len(heights)):
```

```
44          #find the center of the patch
45          tempCenterX = []
46          tempCenterY = []
47          if not fanBeam:
48              for i in np.arange(npatch):
49                  tempCenterX.append(opa[j]
50                  * np.sin(theta[j*npatch + i]))
51                  tempCenterY.append(opa[j]
52                  * np.cos(theta[j*npatch + i]))
53          else:
54              # For the fan beam
55              # same azimuthal angle for all heights
56              for i in np.arange(npatch):
57                  tempCenterX.append(opa[j] * np.sin(theta[i]))
58                  tempCenterY.append(opa[j] * np.cos(theta[i]))
59          centerx.append(tempCenterX)
60          centery.append(tempCenterY)
61      return centerx, centery
62
```

Listing 2.4: The center coordinates of the patches within the beam.

The observed pulsar profiles are a result of an observer's line of sight (LOS) across the pulsar beam. Thus to extract the profile from the beam, it is required to map the rotation phase ϕ onto the observer's plane from which the profile can be generated. The `mapphi()` function (Listing 2.5) maps the pulsar geometry (α, β and ϕ - see Figure 1.3) onto the observer's plane.

```
1   def mapphi(alpha, beta, phi):
2       """
3       Function to map the rotational axis:
```

```
    Args:
    _____
    alpha : magnetic inclination angle w.r.t the rotational
            axis (degrees)
    beta  : line of sight closest approach to the magnetic
            axis (degrees)
    Returns:
    ________
    xlos, ylos  : The coordinates of the rotational plane;
                  both the size of phi.
    """
    cosR = np.cos(np.deg2rad(alpha+beta)) * \
           np.cos(np.deg2rad(alpha))
    cosR += np.sin(np.deg2rad(alpha+beta)) * \
           np.sin(np.deg2rad(alpha)) * np.cos(np.deg2rad(phi))
    R = np.arccos(correct(cosR))
    # problems with precision for 180 degrees
    cosgamma = np.zeros_like(R)
    for i in np.arange(len(R)):
        if int(R[i]*100.0) == 180.0:
            R[i] = int(R[i]*100.0)/100.0
        elif R[i] != 0.0 and R[i] != 180.0 and alpha > 0.0:
            cosgamma[i] = (np.cos(np.deg2rad(alpha+beta)) - \
                           np.cos(np.deg2rad(alpha)) * cosR[i]) \
                          /(np.sin(np.deg2rad(alpha))
                          * np.sin(R[i]))
        else:
             cosgamma[i] = 0.0
    cosgamma_corr = correct(cosgamma)
    gamma = np.arccos(cosgamma_corr)
```

```
34      xp = R * np.sin(gamma)
35      for i in np.arange(len(phi)):
36          if phi[i] > 0.0:
37              xp[i] = -xp[i]
38      yp = -R * np.cos(gamma)
39      # return clockwise los
40      return np.rad2deg(xp)[::-1], np.rad2deg(yp)[::-1]
41
```

Listing 2.5: Function to map the pulsar rotation phase onto an observer's plane of observation.

The line of sight cut across the pulsar beam is determined by the `los()` function (Listing 2.6). The function maps the rotation phase onto an observer's plane using `mapphi()` (Listing 2.5) and extracts the line of sight cut through the plane, given the beam geometry (α and β). The line of sight cut determines the properties (shape, pulse width, etc.) of the intrinsic profile. For example, a tangential cut of a conal beam will result in a single component profile, as opposed to a conal double (Figure 2.1).

The radiation travels from the pulsar magnetosphere and propagates through the ISM where it interacts with electrons. One of the observed effect caused by this interaction is profile scattering which we include in the following section.

```
1   def los(alpha, beta, res):
2       """
3       Function to determine the line of sight cut across the beam.
4       Args:
5       -----
6       alpha       : Inclination angle (degrees).
```

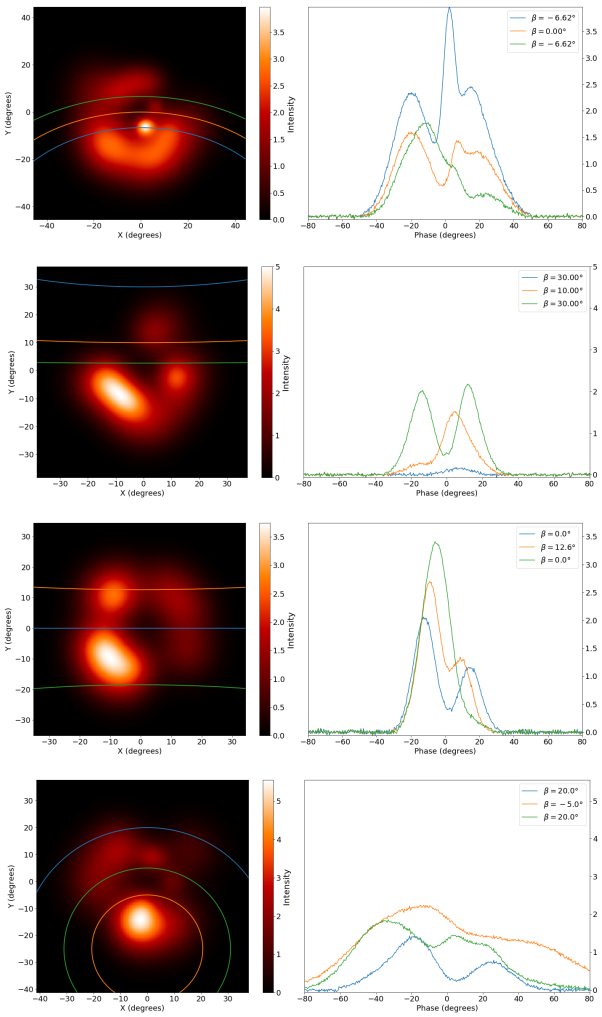

Figure 2.1: Examples of a beam (left of each sub-plot) and possible line-of-sight cut with corresponding profiles (right of each sub-plot). Which part of the beam is observed depends on the beam geometry with respect to the line-of-sight. The observed profile shape depends on where this line-of-sight cut the emission region within the beam.

```
7       beta        : Impact parameter (degrees).
8       res         : Resolution.
9       Returns:
10      ________
11      xlos        : The line of sight x-coordinates (degrees).
12      ylos        : The line of sight y-coordinates (degrees).
13      thetalos    : The line of sight angle in degrees (degrees).
14      """
15  #   rotational phase:
16      phi = np.linspace(-180, 180, num=res, endpoint=True)
17  #   line of sight x,y plane:
18      xlos, ylos = mapphi(alpha, beta, phi)
19      thetalos = np.arctan2(ylos, xlos) * (180 / np.pi) - 90.0
20      thetalos = np.abs(thetalos)
21      return xlos, ylos, thetalos
22
```

Listing 2.6: Function to construct the line of sight (LOS) cut onto the beam.

2.2 Scattering

Fluctuations in the electron densities of the ISM, lead to the frequency-dependent scattering of the radio waves [Williamson, 1972]. This introduces frequency-dependent delays of the radiation to the observer, additional to the dispersive delays associated with the average electron densities along the line of sight. The effect is more pronounced at low frequency where scattering broadens the pulse profiles, producing characteristic scattering tails and also shifts the profile peaks to a later phase. As such, we expect the scattered profiles, generated at low frequencies, to have broader widths with

characteristic scattering tails (e.g Figure 2.2).

To investigate the additional component of the DM caused by intrinsic profile evolution, it is important that we include the scattering effect, as it introduces another DM delay. The observed profile can be well modelled as the result of an intrinsic profile which is convolved with an exponential scattering function $e^{-\Delta t/\tau_s}$ (Listing 2.7) as it propagates through the ISM, where τ_s is the scattering time scale [Löhmer et al., 2004]. The scattering time scale τ_s can be determined for our simulations using Equation 1.4 derived by Bhat et al. [2004] and thus the broadening across a profile from a pulsar with a given period (Listing 2.8) at a specific frequency.

```
1  def sc_time(freq, dm, iseed):
2    """
3    Function to determine the scattering time scale as in
4    Bhat et al. (2004).
5    Args:
6    _____
7    freq    :   frequency (in GHz)
8    dm      :   dispersion measure of the pulsar (pc cm^-3)
9    Return:
10   _______
11   tau     :   the scattering time (in sec)
12   """
13   #tau = scattering time scale as in Bhat et al. (2004)
14   np.random.seed(iseed)
15   # scattering time with added noise term
16   log_tau = -6.46 + 0.154 * np.log10(dm) \
17             + 1.07 * (np.log10(dm))**2 - 3.86 \
18             * np.log10(freq) +  np.random.uniform(-1,1)
```

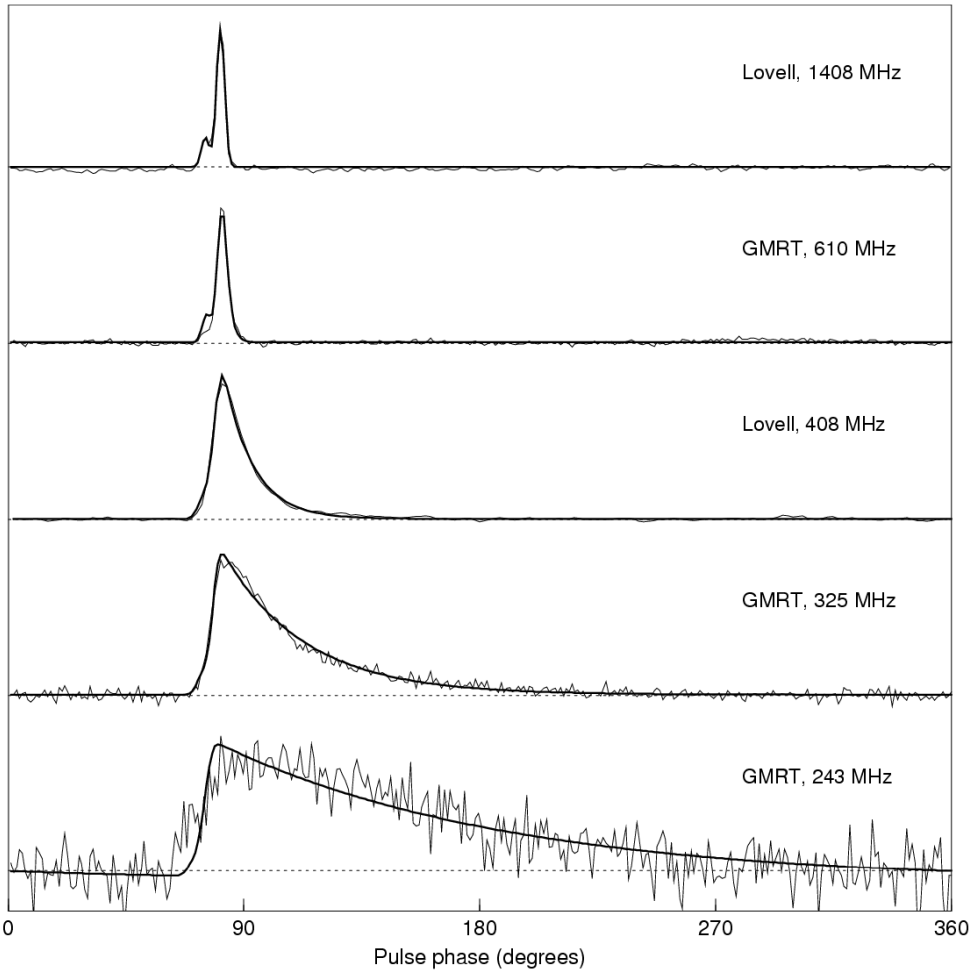

Figure 2.2: The pulse profiles of PSR B1813-03 at multiple frequencies. The profile at the lowest frequency (243 MHz) is more scattered and broader than the profile at higher frequencies(figure from Lorimer and Kramer [2005])

```
    tau = 10**log_tau / 1e3 # (time scale in seconds)
    return tau

```

Listing 2.7: Function that determines the scattering timescale at a given frequency.

```
def broadening(tau, P, res):
    """
    Determine the broadening function
    of the profile due to scattering.
    Args:
    -----
    tau         : scattering time (in seconds)
    P           : period (in seconds)
    Return:
    -------
    broad_func  : broadening function
    """
    t = np.linspace(0, P, num=res, endpoint=True)
    broad_func = 1/tau * np.exp(-(t / tau))
    return broad_func

```

Listing 2.8: Function to determine the broadening function of a profile .

The `pulsetrain()` function (Listing 2.9) constructs a train of pulses from a single pulse profile (Figure 2.3). This step is necessary to include when a high degree of scattering leads to scattering tails that wrap around the full rotational phase of the pulsar. This occurs when a scattering time is a substantial fraction of the pulse period. These pulse profiles are then scattered by convolving them with an exponential function with scattering

tail τ (Listing 2.10). Thereafter, the full-period pulse profile is extracted from the train of pulses (Figure 2.4), using the `extractpulse()` function (Listing 2.11).

```
def pulsetrain(npulses, numberofbins, prof):
  """
  Function to create a train of pulses given a single
  pulse profile.
  Args:
  -----
  npulses        : number of pulses
  numberofbins   : number of bins (resolution)
  prof           : pulse profile
  Return:
  -------
  train          : a train of pulse profiles
                   (size(profile)*npulses)
  """
  binsrange = np.linspace(1, numberofbins, num=numberofbins)
  nbins = np.max(binsrange)
  train = np.zeros(npulses * int(nbins))
  for i in range(npulses):
      startbin = i * nbins
      train[int(startbin):int(startbin + nbins)] = prof
  return train

```

Listing 2.9: Function to create a train of pulse profiles.

```
def scatter(train, bf):
  """
  Function to scatter a pulse profile / a train of
```

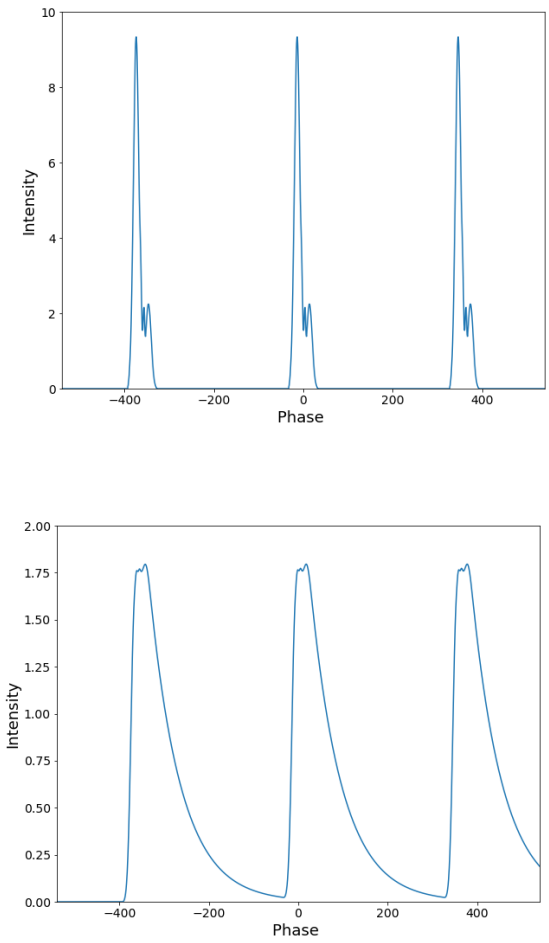

Figure 2.3: An example of a train of 3 pulses (top) reconstructed from a single pulse profile . The step is necessary for cases where there is a high degree of scattering such that the scattering tail wraps around the pulse period. The scattered train is shown at the bottom (scattered with a DM of 80 $\mathrm{pc\,cm^{-3}}$).

```
    pulse profiles.     Returns a convolution of the
    profile with the scattering function.
    Args:
    _____
    pulse   : pulse profile (extracted from a function
              extractpulse())
    bf      : broadening function
    Returns:
    _______
    conv    : scattered profile
    """
    conv = np.convolve(train, bf)
    # normalise the profile:
    profint = np.sum(train) #  area of the profile
    convint = np.sum(conv) #  area of the scattered profile
    sc_prof = conv * (profint / float(convint))
    out = sc_prof[0 : len(train) + 1]
    return out

```

Listing 2.10: Function to create a train of pulse profiles.

```
def extractpulse(sc_train, pulsesfromend, binsperpulse):
    """
    Function that takes the output convolution
    Args:
    _____
    sc_train     : a scattered train of pulse profiles
    pulsefromend : number position of pulse to extract
                   (from the last pulse)
    binsperpulse : number of bins per pulse
```

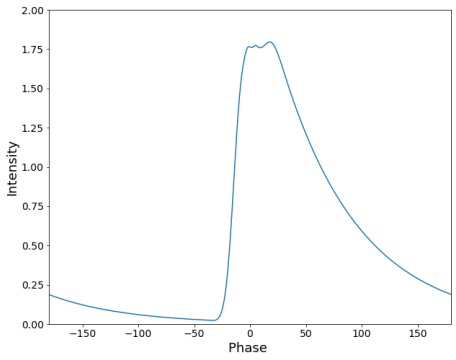

Figure 2.4: A full period scattered profile extracted from a train of the 3 pulse profiles. The middle profile so that it contains the possible wrapping properties available.

```
    Returns:
    ---------
    pulse          : a single pulse profile
    """
    if pulsesfromend == 0:
        start = 0
        end = binsperpulse
    else:
        start = -pulsesfromend*binsperpulse
        end = start + binsperpulse

    pulse = sc_train[int(start):int(end)]
    return pulse

```

Listing 2.11: Function to extract a single scattered pulse from scattered pulse train.

Using the preceding functions, a realistic pulsar beam as well as the line

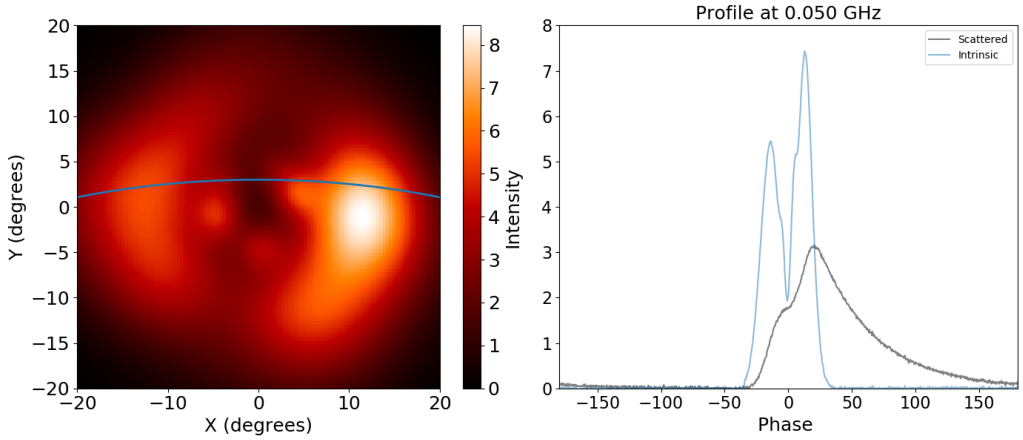

Figure 2.5: An example simulation of the intrinsic conal-patchy beam (left) and LOS cut (blue). The beam is assumed to be observed at 50 MHz, with $\alpha = 30°$ and $\beta = 3°$. The corresponding intrinsic profile from the line of sight is plotted in blue (right) and the observed scattered profile ($DM = 40$ pc cm^{-3}) in grey. The scattered profile peak has been shifted in the forward direction relative to the intrinsic profile.

of sight profiles at given frequency bands can generated. The profiles are assumed to have no dispersive delays - i.e. profiles have already been correctly de-dispersed, hence the only possible source of phase delays in profile features are intrinsic profile evolution and scattering. This phase delay is evident in a plot of the profiles generated across a frequency band (see Figure 3.6).

To investigate how much of this δDM can be assigned to intrinsic profile evolution and scattering, it is required to perform a Monte-Carlo simulation of many pulsars with varying geometry in order to obtain a statistical framework with witch to perform the analysis. The following chapter will this statistical analysis.

Chapter 3

Experiments

The main objective is to investigate the geometric effect of profile evolution, as well as scattering effect, onto the measured pulsar DM. To do so, it is required to make use of the pulsar beam models discussed in Chapter 1 and the simulation code described in Chapter 2 to generate pulsar beams and profiles from which to perform the investigations. The following sections describe the procedure followed to generate pulse profiles and to search for the additional component of the measured DM that is due to profile evolution and interstellar scattering.

3.1 Beam and profile simulation

A profile pulse is generated based on a set of geometric parameters and a beam model (Figure 3.1). Given the pulsar period and the frequency, the probed emission heights can be determined using Listing 2.1. The hollow cone defines a RFM with a single height for a given frequency. The conal-

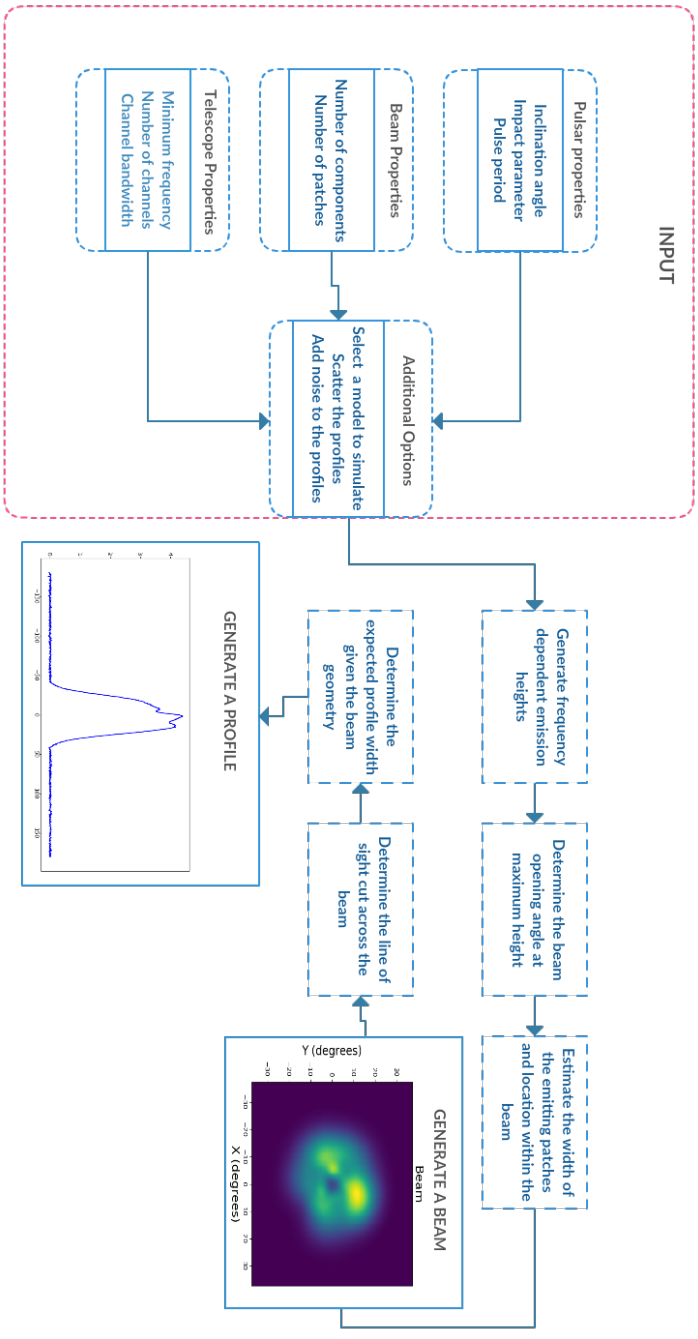

Figure 3.1: An illustrative work-flow chart that shows the steps taken to produce profiles from the beam models.

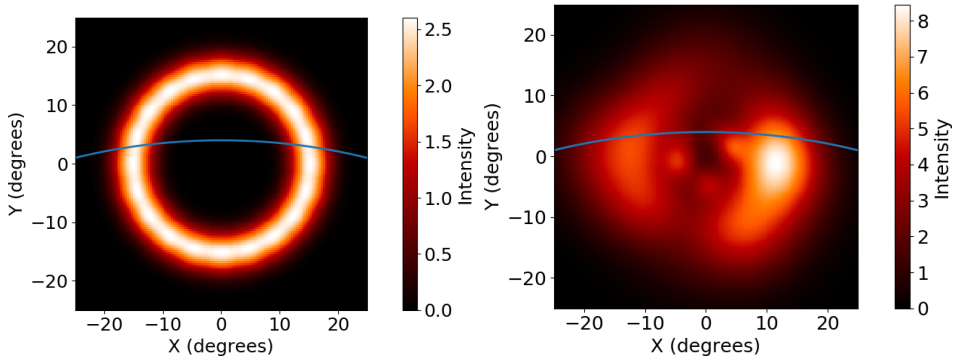

Figure 3.2: Simulated pulsar beams projected onto an XY-plane ($\alpha = 60°, \beta = 3°$). The left plot shows an example beam simulated using the hollow cone beam. The right plot shows an example of a conal-patchy beam. The line of sight cut on the beam is plotted with the blue line, located 3° from the magnetic poles (beam centre [0, 0]).

patchy beam model however proposes that a given frequency can be emitted at multiple heights within the beam to introduce the multiple profile components.

With the emission heights and the pulsar period, the widths of the discrete emitting regions (or patches) within the beam are generated using Listing 2.2 & 2.3). Given α and β, the line of sight cut onto the beam is determined using the functions in Listing 2.5 & 2.6 (plotted with blue line on the beam in Figure 3.2).

The intrinsic profiles are extracted from regions where the line-of-sight cuts through the beam. The expected maximum profile width (maximum width at lowest frequency in the band, assuming the beam is fully illuminated) for the given geometry can be estimated using Gil et al. [1984]

$$\sin^2\left(\frac{W}{4}\right) = \frac{\sin^2\left(\frac{\rho}{2}\right) - \sin^2\left(\frac{\beta}{2}\right)}{\sin\alpha \sin\left(\alpha+\beta\right)}, \tag{3.1}$$

An example of the generated profiles from the hollow cone and conal-patchy beam models are shown in Figure 3.3.

Figure 3.4 shows a sequence of 10 profiles generated between 50MHz at the bottom and 350MHz at the top. The peaks of the profiles at low frequencies are shifted in phase relative to the profiles at the higher frequencies. This intrinsic profile shift resembles the dispersive delays introduced by the interstellar dispersion discussed in Chapter 1 (Figure 1.7). The intrinsic profile phase shift, due to profile evolution, can be misinterpreted as interstellar dispersion, embedded in a pulsar DM. As such, the intrinsic phase shift is interpreted as an additional component to the ISM induced DM, caused mainly by profile evolution across wide bands.

3.2 Scattering

The resultant intrinsically delayed waves travel through the ionised ISM where they interact with electrons. The frequency dependent index of refraction slows the group velocity of the waves further (Equation 1.3), an effect that is more pronounced at low frequency. In addition to the dispersive delays, propagation through the inhomogeneous ISM causes frequency dependent multipath propagation, where the waves are scattered in such a way that frequency dependent broadening effect is introduced in the observed profile (another effect that is more pronounced at low frequencies).

Thus, to scatter the intrinsic profiles, profiles corrected for the true dispersive delay are assumed, and convolved with an exponential scattering function (Listings 2.8 and 2.10) with a scattering time scale as given in Equation 1.4.

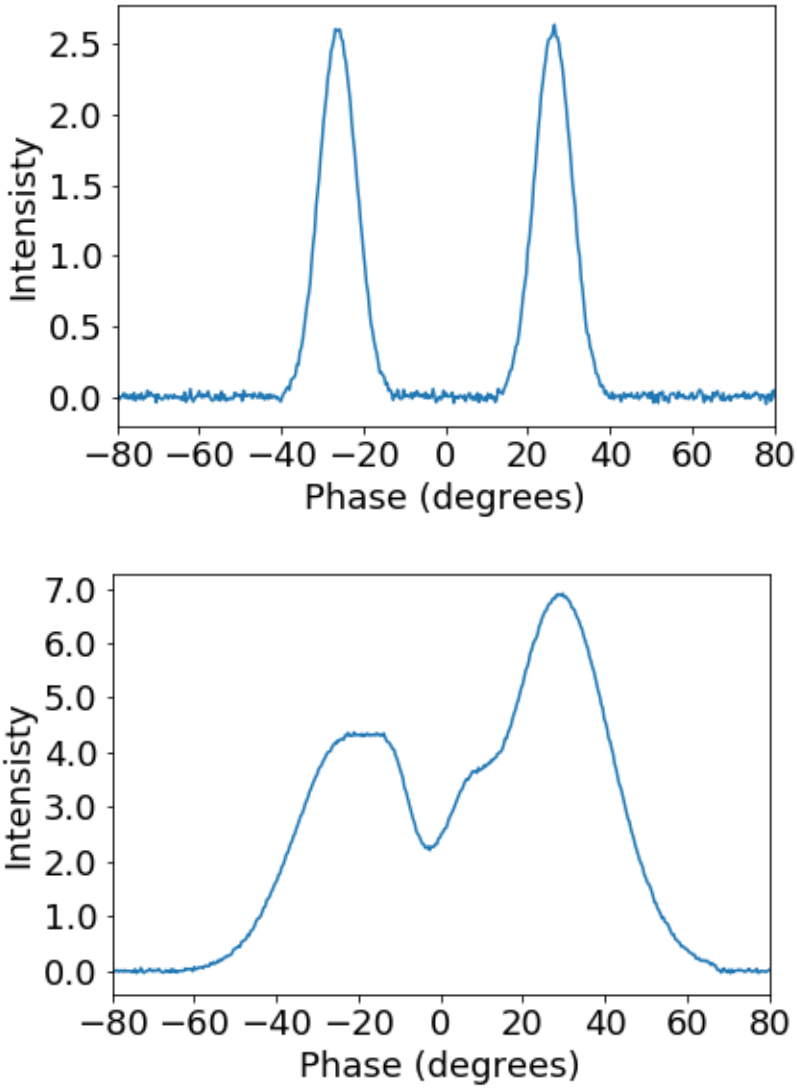

Figure 3.3: Examples of profiles generated from the beams in Figure 3.2. The top profile is from the hollow cone beam and on the bottom profile is the conal-patchy beam.

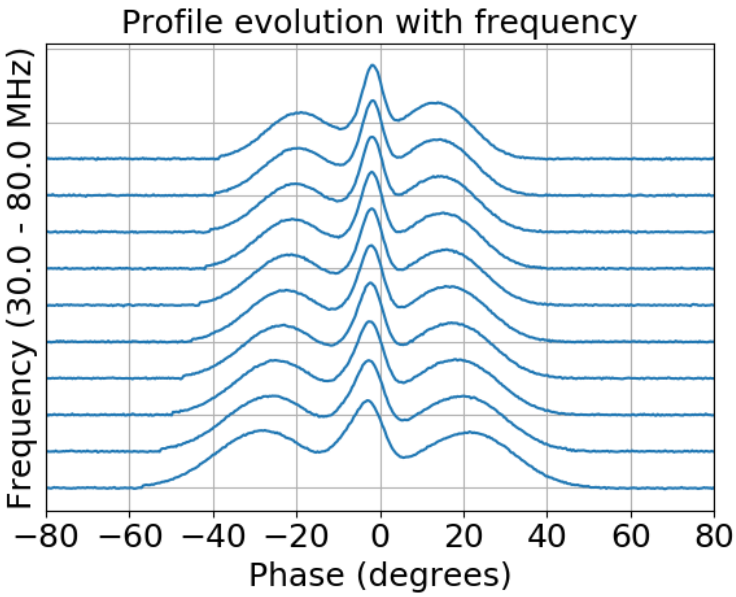

Figure 3.4: Example of profiles at 10 frequencies, generated from using the conal-patchy beam for a P = 1 s between 30 - 80 MHz (frequency increases from bottom profile to top) after propagation through the ISM.(frequency increases from bottom to top). Note, the apparent offset in the peak at different frequencies is intrinsic to the beam model.

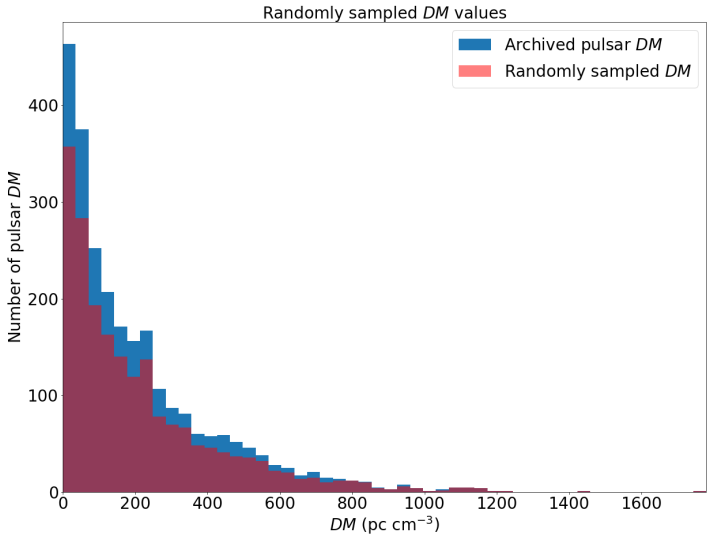

Figure 3.5: A histogram showing known pulsar DM from the catalogue (blue) with the randomly resampled DM (red). See text for further description.

Here a parameterized DM for scattering is included; for the purpose of the simulations, the known DM values of real pulsars in the ATNF catalogue are used. A probability distribution of these known pulsar DMs is determined, and is randomly sampled for a DM to use for the scattering routine. Figure 3.5 shows a histogram of the known pulsar DM from the catalogue (blue) with the resampled DM distribution (red). A DM is randomly sampled from the distributions, and applied to Equation 1.4 to determine the possible scattering time-scale. An example of the result of this is shown in Figure 3.6 which represents a simulation of the same profiles in Figure 3.4 after including scattering effects.

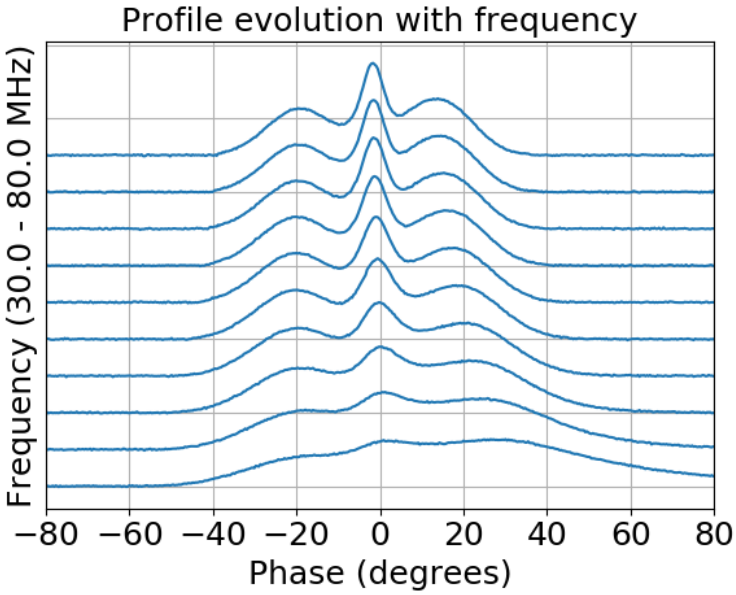

Figure 3.6: Example profiles in Figure 3.4 after applying scattering effects. It is initially assume that the profiles are corrected for the dispersive delays with a correct DM. The scattered profiles are produced by convolving the intrinsic profiles with an exponential function with a tail defined by the scattering time scale $\tau \propto \nu^{-4}$ with $\tau = 7.9 \times 10^{-2}$s at 30 MHz.

3.3 δDM search

The peaks of the generated profiles (see Figure 3.4 and 3.6) exhibit relative shifts in phase. This shift is due to intrinsic profile evolution as seen in Figure 3.4, from the height-dependence origin of profiles at different altitudes when observed at different frequencies (the RFM) and a combination of scattering as seen in Figure 3.4 & 3.6.

This relative phase shift is interpreted as an additional component of the DM that is due to geometric profile evolution with frequency, which I refer to from here as δDM. To search for this δDM, the highest frequency profile is taken as a reference profile and is used to determine a time delay that would shift the profiles across the whole pulse width. A broad DM bin range is searched within this pulse width for a δDM that maximises the peak of the average profiles. For each of the δDM in the range, the other profiles are shifted relative to the reference profile and are averaged after each shift to obtain an average profile. For all the trials in a range, the δDM that maximises the peak of the average profile is selected as the best δDM (Figure 3.7). A second iteration of a fine search around the selected value is performed, where the "best δDM" is selected as the DM that again maximises the peak amplitude of the average profile after the second iteration (zoomed region in Figure 3.7).

For comparison, a template-matching method as described in Section 1.2 is also used to obtain an alternative δDM. A noiseless, high-frequency profile in the band is selected as a template and is cross-correlated with the rest of the profiles to determine the relative delays, which are then translated to δDM by fitting Equation 1.3 (see Figure 3.8). It can be seen from the fit

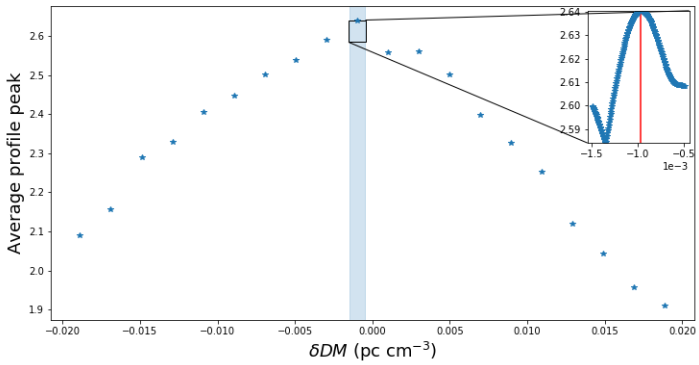

Figure 3.7: An example of the frequency-averaged peak for the δDM search during the 'coarse' first iteration - the shade region shows the area selected to do a 'fine' second iteration (zoomed in plot). The selected best δDM is indicated with a red line as shown in the zoomed plot ($\delta DM = -1.9 \times 10^{-3}$pccm^{-3} for this example).

(bottom plot of each panel in Figure 3.8) that although this δDM mimic the ISM DM, it does not exactly follow the ν^{-2} law expected from interstellar dispersion.

3.4 Monte Carlo population sampling

Figure 3.1 shows the steps taken to produce the simulated pulsar beams and profiles. The framework allows the user to select pulsar properties (α, β and P), the properties of the beam (number of patches of emitting regions and the number of multiple heights per frequency), the telescope properties (the observing frequency band and number of channels to simulate for) as well as additional options (to select a model for the simulation, to include scattering and random noise onto the profiles).

To perform a Monte Carlo simulation of the pulsar populations, this work

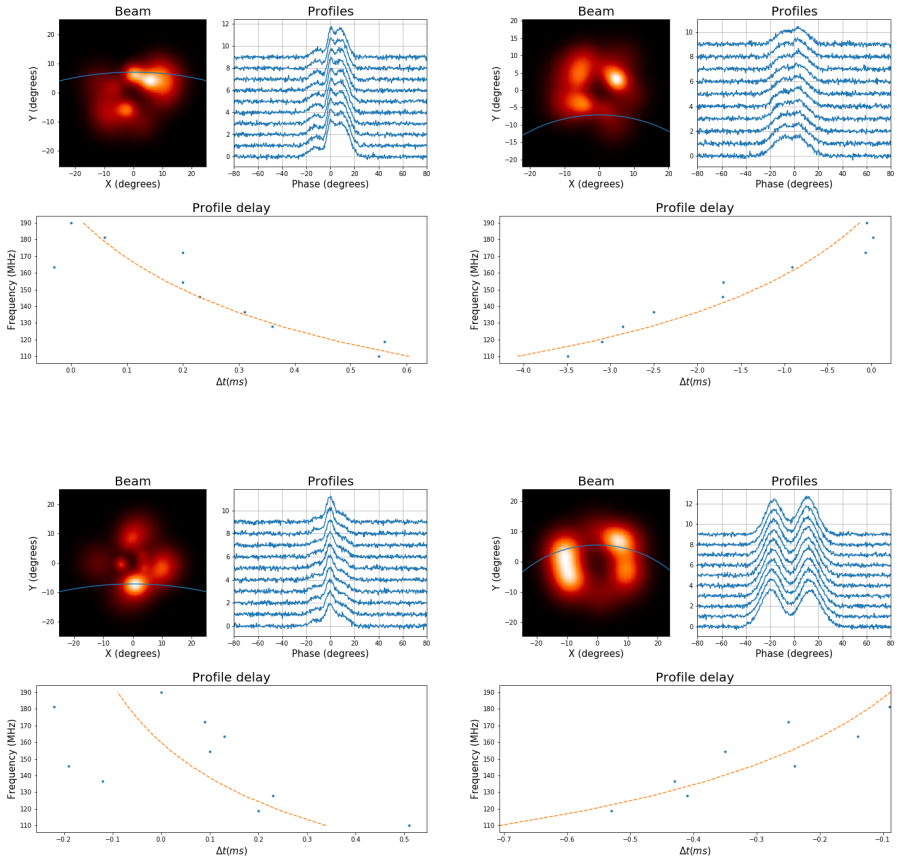

Figure 3.8: Examples of fitting δDM curve using the template matching method. The figure shows various examples of a simulated beam (top left) and the corresponding profiles (top right). The bottom plot shows the corresponding time delays between the profiles and a template (blue dots), as well as a fit of the δDM curve (orange dashed line).

flow is iterated by randomly sampling the pulsar geometry properties (α and β) and observing frequency band. Table 3.1 shows the parameters used for the experimental set-up. Only slow pulsars are simulated, specifically those with $P = 1$s. Moreover, the simulate profiles are assumed to be observed with broadband receivers typical of today's instruments and those planned for the future.

Only the part of the pulsar beam that would be pointed in the observer's line-of-sight is simulated. To ensure this, β is selected such that it lies within the maximum size of the beam (ρ at lowest frequency in the band). This is so that pulsars with either small or large β, with profiles still in line-of-sight, can be simulated. The beam inclination angle (α) is randomly sampled between 0 - 90 degrees. In the case of possible orthogonal rotators (where $\alpha \approx 90$ degrees), only emission from one pole is simulated[1].

For the purpose of investigating the effect of intrinsic profile evolution, frequency bands that resembles those in current and future broadband telescope receivers are selected (Table 3.1). For low frequency receivers I decided to simulate intrinsic pulse profiles for the LOFAR receivers (LBA at 30 - 80 MHz with $f_{bw} \approx 91\%$, and HBA at 110 - 190 MHz with $f_{bw} \approx 53\%$) as well as the planned future SKA-Low band at about 50 - 350 MHz which will have $f_{bw} \approx 150\%$. At these low frequencies, more pronounced ISM effects are expected (possible delays due to profile scattering and dispersive delays, and thus visible profile evolution is expected). I also simulate for the currently commissioned MeerKAT L-Band receiver at 850 - 1700 MHz with $f_{bw} \approx 67\%$. In this band, little to no profile evolution has been observed in many pulsars.

[1]This is for simplicity, as well as to refrain from making assumptions such as assuming that the two beams from both magnetic poles are either identical or different.

Table 3.1: Experimental parameters used for the simulation. The same parameters were used for both beam models.

Parameters	**values**
Period (s)	1.0
α (degrees)	[0, 90]
β (degrees)	[-ρ, ρ]
Emission altitude (km)	[20, 500]
RFM index	$\nu^{-0.95}$
Frequency bands (MHz)	[30, 80] [110, 190] [50, 350] [850, 1700]
Number of frequency channels	10

PSR B1133+16 is an example of such a pulsar where the profiles shows little evolution above 1 GHz [Thorsett, 1991].

To generate the profiles the selected parameters for the pulsar geometry are used, as well as the observing frequency and the pulsar model to use for the simulation. The pulsar models discussed in the previous chapters attribute the profile width and evolution with the height of emission at a given frequency through the RFM model. The fan-beam model however suggests that the beam emits all frequencies across a large height range, which does not provide a clear picture of the origin of the height-frequency relationship observed. Thus for the purpose of this experiment it was decided to proceed with only the hollow cone and the conal-patchy beam models for our simulations and experiments.

For the KJ07 beam model, a small number of components, arising from the expectation that the same frequency can be emitted from multiple heights,

is simulated. The beam is populated by patches that are randomly distributed (see Karastergiou and Johnston [2007]). For the hollow cone model there is only one height of emission for each frequency. The radiating ring of the cone is assumed to be illuminated by many patches (we chose 20 patches to form a uniform conal ring) that are distributed azimuthally along the cone to form a ring of emission at a distinct height for a given frequency.

As many pulsars as 1000 normal pulsars ($P = 1$ s pulsars) with random beam geometry, are simulated at a given band for each of the selected models. The intrinsic average pulse profiles (with added Gaussian noise) in the frequency band are simulated using the code described in the previous chapter. For each of the pulsar profile δDM is searched following the steps discussed above. The same procedure is repeated again, this time with the option to include scattering effect. Each experiment in the band produces a δDM distribution. This distributions are presented in the following chapter.

Chapter 4

Results

Chapter 3 discussed the simulation procedure to produce the pulse profiles for various pulsar geometries. This chapter presents the δDM distributions resulting from the Monte-Carlo population simulations, for each of the models at the frequency bands presented in Chapter 3. Firstly, the experiments investigating the effects of intrinsic profile evolution are presented, followed by the realistic representation of the measured profile evolution by including scattering effects, and finally the results are interpreted.

4.1 δDM Distributions: Intrinsic

The intrinsic profiles simulated in the preceding chapter exhibit a relative shift in phase across frequencies. The profile in Figure 3.4 at the lowest frequency (50 MHz) peaks at a slightly earlier phase relative to the peak of the profile at maximum frequency in that band (350 MHz). This phase shift is attributed to the height dependent frequency of emission as explained by the

RFM model in Section 1.1.1 The profile phase shift, due to RFM, can be in the opposite direction to the shift caused by the ISM dispersive delay (Figure 1.7). Such a negative delay has been observed in some pulsars by Ahuja et al. [2007]. In the statistical simulations in Chapter 3 the corresponding δDM to the aforementioned delay is searched for using a Monte-Carlo simulation of the pulsar population with varying geometries. Figures 4.1 and 4.2 show distributions of δDM computed from simulations using the hollow cone and conal-patchy beam model, respectively, in various bands.

The low-frequency distributions for the hollow cone beam model (Figure 4.1: LBA, HBA and SKA1-Low) show evidence of the symmetric double component profiles generated from the model. A zero δDM is expected from profiles that are symmetric or if profiles do not follow the RFM model, i.e. if the profiles do not show evidence of evolution with frequency. The double component symmetry in the distribution implies equal probability of finding a positive or negative δDM. The distributions from the conal-patchy model (Figure 4.2), on the other hand, show plenty of zero δDM examples. These are a result of emission patches that lie on the plane of the rotation and magnetic axis.

The δDM scale of the distributions from both models look similar. For example the low-frequency distributions (LBA) in Figures 4.1 and 4.2 show small δDM values, ranging between -2×10^{-2} pc cm^{-3} and 2×10^{-2} pc cm^{-3}, as opposed to the high-frequency band (L-Band in figs. 4.1 and 4.2) which range between -3 pc cm^{-3} and 3 pc cm^{-3}.

From the quadratic frequency-dependent time delay equation (Equation 1.3), it is expected that a higher dispersive delay will be measured for a given DM,

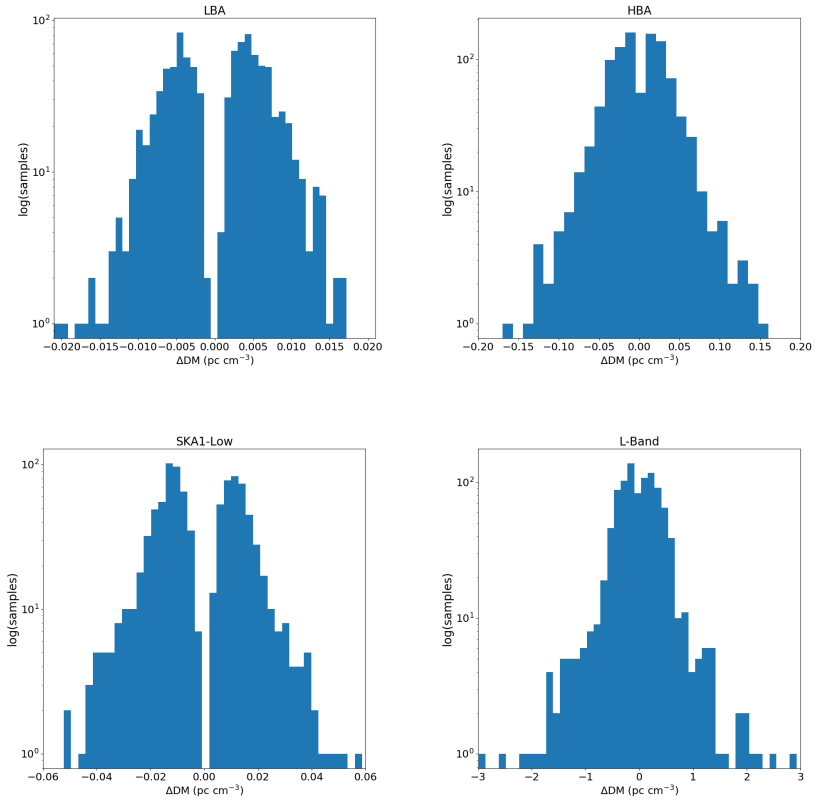

Figure 4.1: The δDM distribution of 1000 pulsars simulated using the hollow cone beam model at various bands. The top left plot shows the results at 30-80 MHz (LBA) and top right at 110-190 MHz (HBA). The distribution at 50-350 MHz (SKA-Low) is shown on the bottom left and 850-1706 MHz (L-Band) on the bottom right.

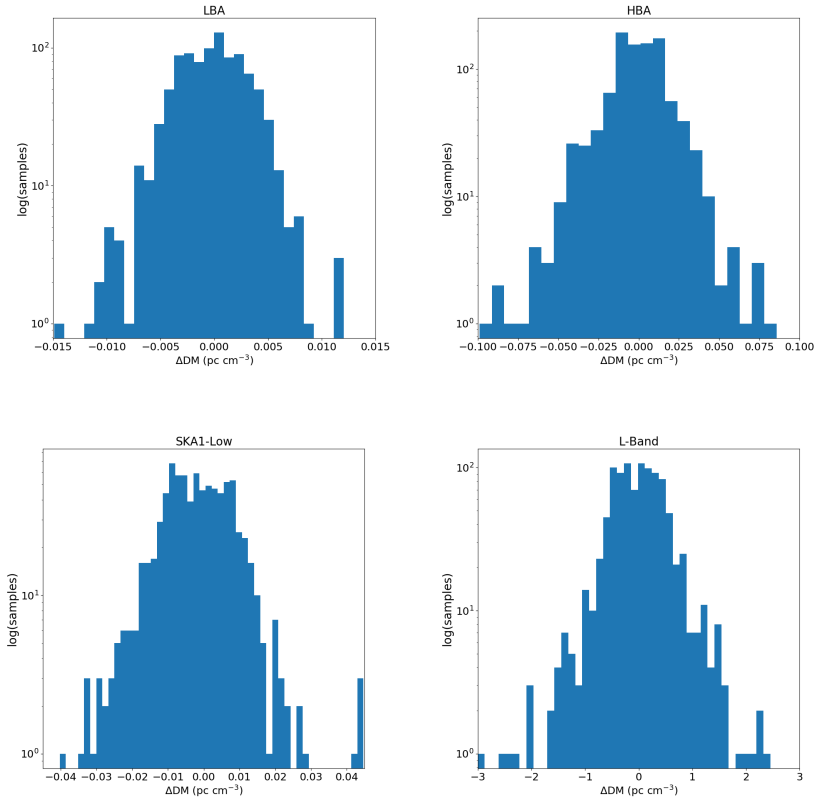

Figure 4.2: The δDM distribution of 1000 pulsars simulated using the patchy-conal beam model at various bands. The top left plot shows the results at 30-80 MHz (LBA) and top right at 110-190 MHz (HBA). The distribution at 50-350 MHz (SKA1-Low) are shown on the bottom left and 850-1706 MHz (L-Band) on the bottom right.

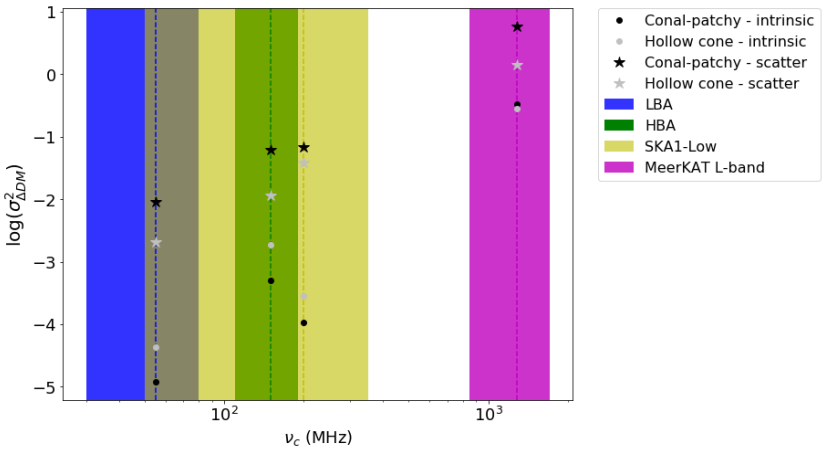

Figure 4.3: The variance of the δDM distributions per frequency for the two beam models. Values from the hollow cone beam model simulations are represented in grey and the conal patchy beam model simulations in black. The circles represent the variance from the intrinsic profile simulations and the stars represent the scattered profile simulations. The bands for which both the beam models are simulated are indicated by the shaded areas (blue represent the LBA-like frequencies, green the HBA-like frequencies, yellow the planned SKA1-low frequencies and magenta represent the MeerKAT L-band) with their corresponding centre frequencies represented by the dashed lines.

at lower frequencies. This measured DM is defined as an interstellar effect caused by the electron density in the ISM which interacts with radio waves from the pulsars.

Although the higher frequency profiles show little to no evolution, the statistical simulations above indicate that a broader δDM distribution is expected intrinsically. The explanation is simple - at high frequencies, even a small phase shift across the band (caused by RFM), will correspond to a rather high DM, and at low frequencies, the opposite is true - even a large phase shift may correspond to a small DM. This explains the high δDM distribution values in the high frequency band (e.g. the L-Band distributions Figures 4.1 and 4.2), which imply that a small relative profile shift in such a band will introduce a relatively large δDM.

To understand this result, we can assume we have profiles observed at two frequency bands (e.g. centered at $\nu_{c(low)} = 55$ MHz and $\nu_{c(high)} = 1200$ MHz), over the same bandwidth BW. The measured time delays across the band at the low and high frequencies will be:

$$\Delta t(\nu_{low}) \propto BW * (55 \text{ MHz})^{-3} DM_{\nu_{low}} \tag{4.1}$$

and

$$\Delta t(\nu_{high}) \propto BW * (1200 \text{ MHz})^{-3} DM_{\nu_{high}} \tag{4.2}$$

respectively. Therefore it requires a $DM_{\nu_{high}} > DM_{\nu_{low}}$ to shift the profiles at high frequency such that the time delays $\frac{\Delta t(\nu_{low})}{\Delta t(\nu_{high}} = 1$. Similarly, a large δDM is required to cause a small shift in the high frequency intrinsic profiles.

This effect is therefore more pronounced at high frequencies, suggesting

Table 4.1: The fractional bandwidth for each of the bands used in the simulations.

Band	**Fractional bandwidth**
LBA	0.91
HBA	0.53
SKA1-low	1.50
MeerKAT L-Band	0.67

that an observed pulsar DM will include an excess δDM that is larger at high frequency than when observed at low frequency. To investigate the frequency dependence of this excess dispersion measure we look at the different frequency bands and fractional bandwidths. Figure 4.3 shows the spread of δDM distribution with centre frequency for both emission models. The black and grey circles represent the variance per frequency band for intrinsic profiles simulated with the conal-patchy and the hollow cone beam models respectively. The shaded regions indicate the bandwidths used for the simulations, for which the centre frequencies are indicated by the corresponding vertical dashed lines.

Looking at the black and grey circles, notice that at the LBA-like band (30 - 80 MHz) the variance is smaller than at the MeerKAT-like band (850 - 1706 MHz). The small δDM variance at this high frequency band can also be regarded as a consequence of the presence of the large δDM at high frequencies. The intrinsic profile evolution therefore has an opposite frequency dependence to the ISM induced delays discussed in Chapter 1.

Ahuja et al. [2007] observed the DM variations with frequency for PSRs B1642-03 and B0329+54. They note that the DM measurements for these pulsars were larger at higher frequencies compared to low frequency values,

which they also attributed to the frequency-dependent emission height in the pulsar magnetosphere.

4.2 δDM distribution: scattering

If the beam geometry in Chapter 1 and RFM model are assumed the correct models of the pulsar emission frequency with height, this means then that despite which pulsar beam model used the pulsars geometry will introduce an additional component to the measured ISM DM. It is discussed in Chapter 1 that scattering can introduce an additional component to the measured DM as well. This results from the fact that pulse profile broadening due to scattering can shift the profile peak, causing a relative shift in the low-frequency profiles across the band. Figures 4.4 and 4.5 show distributions of δDM with scattering included, simulated using the hollow cone and the conal-patchy beam models, respectively.

Profile scattering due to the multipath propagation of the pulsar waveform through the ISM shifts the profiles peak in the positive direction. As such, it is expected that the δDM distributions in the simulation with scattering included, will manifest a feature that resembles the forward exponential tail that is observed in scattered profiles (see Chapter 1) as opposed to the relatively symmetric distributions of the intrinsic profile simulations in Section 4.1.

The scattering feature can be seen in Figures 4.4 and 4.5 distributions where it manifest itself as the positive skewness of the distributions. Here the first thing to notice is that the gaps at zero δDM (observed in the

low-frequency distributions for the hollow cone beam model - Figure 4.1 : LBA, SKA1-low and HBA) due to the symmetric nature of the double component profiles generated from the model has been masked the additional peak shifts caused by scattering (Figure 4.4). Secondly, the δDM range of the distributions with scattering effect are larger than those from the intrinsic distribution, putting emphasis on the fact that scattering can also introduce additional component to the measured pulsar DMs. At low frequencies where profiles are highly scattered, disentangling the scattering effect from intrinsic profile evolution may be difficult [Geyer et al., 2017].

The above feature can also be observed in Figure 4.3 where the variance from scattered distributions are indicated by the black and grey stars for the conal-patchy and the hollow cone beam models respectively. It is evident from this figure that the variance of the scattered distributions have increased relative to the intrinsic distributions. For example, the scattered LBA δDM distribution range from the hollow cone beam model (Figure 4.4) increased by a factor of about 50 from that intrinsic δDM range (Figure 4.1), and the MeerKAT δDM increased by a factor of 4. This indicate that the measured pulsar DM contains not only the intrinsic δDM due to profile evolution but also contains an additional component due to interstellar scattering. Therefore, δDM at low frequency will be dominated by scattering whereas profile evolution will dominate at high frequency. It can also be seen from the plots of δDM distributions determined using the template-matching method that this intrinsic effect does not follow the ν^{-2} law (Figure 3.8).

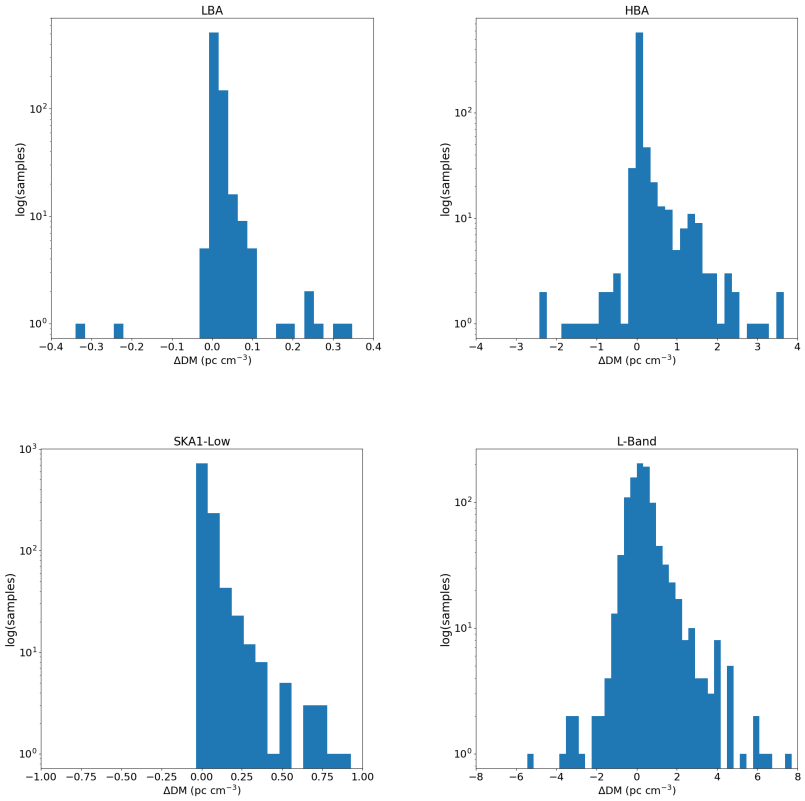

Figure 4.4: The δDM distribution of 1000 pulsars simulated using the hollow cone beam model at various bands with scattering effects included. The top left plot shows the results at 30-80 MHz and top right at 110-190 MHz. The distribution at 50-350 MHz are shown on the bottom left and 850-1706 MHz on the bottom right.

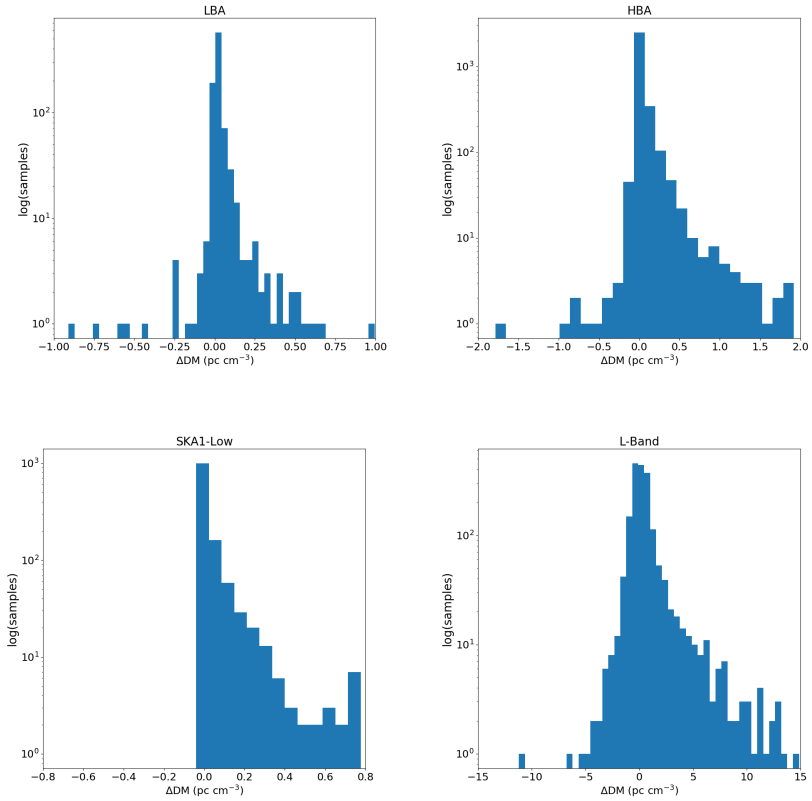

Figure 4.5: The δDM distribution of 1000 pulsars simulated using the patchy-conal beam model at various bands with scattering effects included. The top left plot shows the results at 30-80 MHz and top right at 110-190 MHz. The distribution at 50-350 MHz are shown on the bottom left and 850-1706 MHz on the bottom right.

Chapter 5

Discussions

The current pulsar catalogue contains DMs measured at various frequency bands. Many of these DMs has been measured during the pulsar search surveys using data collected with narrow band receivers. However, future survey are planned to use sophisticated instruments (e.g. LOFAR, MeerKAT and the SKA) which will allow observations across wide-frequency bands. In radio pulsar astronomy this is particularly important because, although pulsars are weak radio sources, they emit radio waves over a broad band.

Using broadband receivers for pulsar observations will introduce systematic errors such as those discussed in the preceding chapter. The results presented above indicate that the use of broadband pulsar data will introduction an excess δDM on the measured pulsar DMs. We discover in the discussions above that this excess δDM imply that a pulsar DM determined at low frequency band may not be a correct representation of the same pulsar DM at high frequency band when using broadband receivers. It is also observed that at the low frequency band, the excess δDM is dominated by

scattering effect, whereas a larger excess δDM at high frequency is introduced by profile evolution. Thus, it will be important to take the results above into consideration, especially for pulsar timing where taking into account all the possible contributions to DM errors and possible variations is required for TOA measurements with high precision.

With this experiment, it is clear that there are three possible effects that can contribute to the measured dispersive delay.

I. **Intrinsic profile evolution**: The RFM model suggests height dependent emission in the magnetosphere, with high frequencies emitted at lower emission heights and low frequencies at higher heights. As the pulsar rotates, the low frequency waves emitted at high altitudes are directed onto the line of sight earlier than the high frequency waves from lower altitudes. Thus the peaks of the pulse profiles at low frequencies and high frequencies are misaligned, introducing a $\delta DM_{geometric}$ which is a geometric effect. This effect is separate from the retarded light travel time between emission heights at multiple frequencies ([Phillips, 1992] has found retardation time to have little to no effect in the TOA), but is purely a geometric effect.

II. **Interstellar dispersion**: The misaligned intrinsic pulses then travel through the ionised ISM where they interact with the free electrons. The group velocity of the waves experience a frequency dependent delay during propagation, where low frequency pulses are delayed more that high frequency pulse upon arrival to the telescope. This dispersive delay $DM_{dispersition}$ is associated with the electron column density in the line of sight and contain the excess $\delta DM_{geometric}$ from profile evolution.

III. **Scattering**: In addition to the frequency dependent dispersive delay, the inhomogeneous nature of the ISM causes a multi-path propagation of the radiation that is also frequency dependent. The resultant waves are scattered with the effect more pronounced at low frequencies, and therefore broadening the resultant profiles and shifting the peaks in a forward direction. This misalignment introduces an additional excess $\delta DM_{scattering}$.

Thus the measured DM contains a contribution of the above effect as

$$DM = DM_{dispersion} + \delta DM_{geometric} + \delta DM_{scattering}. \tag{5.1}$$

It is important to remember that a measurable parameter here is the time delay between profiles in the band. The dispersive delay is related to the observing frequency using Equation 1.3, where DM is a parameter that is inferred from the delay and is defined as the ISM electron column density in the line-of-sight. Frequency dependent variations of the effects described above, due to scattering and profile evolution, mimic interstellar DM in such a way that they can be misinterpreted as due to the ISM when using broadband data.

For high precision pulsar timing, especially for PTAs where data from multiple instruments with various frequency bands and fractional bandwidths will be compared, the results above are essential. They indicate that DM measured at high frequency bands will have excess dominated by profile evolution ($\delta DM_{geometric}$) whereas low frequency DM will be dominated by scattering ($\delta DM_{scattering}$). For constant scattering and profile evolution, these

effects will be absorbed and may not be visible. However, for variable profile evolution (if the pulsar beam/beam geometry varies in time) and scattering (scattering variations due to turbulent ISM and line-of-sight changes with time), this effect will strongly affect the long term monitoring of the pulse TOAs.

Thus, it is necessary that the planned wide-band instruments do no depend on the pre-determined pulsar DMs measured using narrow-band receivers as this will introduce errors in the analysis when applied to broad-band data. However, the effect discussed above depends on the average pulsar profiles and thus represents an average effect. Single pulses from pulsars have shown various frequency-dependent behaviours that may also be important. Some pulsars display a behaviour characterized by single pulses in a given band switching "on" and "off" for a short period [Backer, 1970]. Other pulsars have single pulses that display a drift in phase across frequency band [Hassall et al., 2013]. These shifts could also produce a net effect. This could constitute the topic of further work.

The analysis is also dependent on the assumption that profile evolution is due to the RFM model where emission frequency is dependent on the altitude from which radiation in the pulsar magnetosphere is beamed as well as that asymmetric profiles. In general, most pulsar profiles are asymmetric. However, not all pulsars can be modelled by the RFM model; PSR J0630-2834 is a single component profile that does not display evolution with frequency and PSR J0837+0610 is a double component profile whose width seems to get narrow at low frequency [Xue et al., 2017]. For these pulsars, intrinsic profile evolution might not introduce a large excess DM, however, scattering

can still introduce significant excess DM at low frequency.

Similar behaviour has also been observed in PSR J2145-0705 which does not follow the expectation of the RFM model [Bailes et al., 1994]. This pulsar's profiles width decrease with decreasing frequency. Kuzmin and Losovsky [1996] perform an analysis to explain the profile width evolution of this pulsar by suggesting that the structure of the magnetic field for this pulsar must be quadrupolar, instead of dipolar as is defined by the RFM and pulsar beam models presented above in the preceding chapters. As such, it is therefore without a doubt that understanding the nature of the pulsar magnetosphere is necessary to explain many observed pulsar phenomena.

Chapter 6

Conclusion

In the preceding chapters, the effect of intrinsic profile evolution as well as extrinsic effect of scattering on the measured ISM induced pulsar DM are investigated. I propose that when using broad-band data, these two effects (profile evolution and scattering) will contribute an excess δDM embedded in the ISM induced DM.

To test this proposal, I made use of pulsar beam geometry and the radius-to-frequency (RFM) model incorporated in the pulsar beam models (the hollow cone and conal-patchy beam models) to generate average profiles channelised in wide-frequency bands typical to those observed with telescopes today or those that will be observed with planned future wide-band receivers. I performed a Monte-Carlo simulation of the pulsar population with varied pulsar beam geometry for each model, from which average pulse profiles, assessed at several frequency bands, were generated.

The generated pulsar profiles in a given band exhibit a relative phase shift due to intrinsic profile evolution with frequency and scattering where

included. The shift from both these effect is interpreted as an additional component to the DM, represented by δDM. The contribution due to profile evolution is found to dominate δDM at high frequency. This surprising result comes as a result of the expected height dependent frequency of emission explained by the RFM model. The high frequencies, which are emitted at lower altitudes in the magnetosphere, relative to the low frequencies from the same pulsar beam, will have a steeper gradient. As such, a small relative profile shift at these frequencies will contribute a larger δDM than the same shift at low frequency profiles. However, when the same pulses propagate through the ISM, they are less scattered than the low frequency. Therefore, it was found that the δDM excess is dominated by scattering effect at low frequency and intrinsic profile evolution dominates at high frequency.

The measured pulsar DM contains then contribution from both the intrinsic components (intrinsic profile evolution) as well as extrinsic effects (ISM induced dispersive delays and scattering). This will be of concern for high precision pulsar timing using wideband data where small variations and errors of the pulsar parameters measure (DM in our case) can cause large errors in the pulsar timing measurements.

Bibliography

A. L. Ahuja, D. Mitra, and Y. Gupta. The effect of pulse profile evolution on pulsar dispersion measure. MNRAS, 377:677–686, May 2007. doi: 10.1111/j.1365-2966.2007.11630.x.

D. C. Backer. Pulsar Nulling Phenomena. Nature, 228:42–43, October 1970. doi: 10.1038/228042a0.

D. C. Backer. Pulsar average wave forms and hollow-cone beam models. ApJ, 209:895–907, November 1976. doi: 10.1086/154788.

M. Bailes, P. A. Harrison, D. R. Lorimer, S. Johnston, A. G. Lyne, R. N. Manchester, N. D'Amico, L. Nicastro, T. M. Tauris, and C. Robinson. Discovery of three binary millisecond pulsars. ApJ, 425:L41–L44, April 1994. doi: 10.1086/187306.

N. D. R. Bhat, J. M. Cordes, F. Camilo, D. J. Nice, and D. R. Lorimer. Multifrequency Observations of Radio Pulse Broadening and Constraints on Interstellar Electron Density Microstructure. ApJ, 605:759–783, April 2004. doi: 10.1086/382680.

A. V. Bilous, J. W. T. Hessels, V. I. Kondratiev, J. van Leeuwen, B. W.

Stappers, P. Weltevrede, H. Falcke, T. E. Hassall, M. Pilia, E. Keane, M. Kramer, J.-M. Grießmeier, and M. Serylak. LOFAR observations of PSR B0943+10: profile evolution and discovery of a systematically changing profile delay in bright mode. A&A, 572:A52, December 2014. doi: 10.1051/0004-6361/201424425.

J. M. Cordes. Observational limits on the location of pulsar emission regions. ApJ, 222:1006–1011, June 1978. doi: 10.1086/156218.

J. M. Cordes, R. M. Shannon, and D. R. Stinebring. Frequency-dependent Dispersion Measures and Implications for Pulsar Timing. ApJ, 817:16, January 2016. doi: 10.3847/0004-637X/817/1/16.

A. A. Deshpande and J. M. Rankin. Pulsar Magnetospheric Emission Mapping: Images and Implications of Polar CAP Weather. ApJ, 524:1008–1013, October 1999. doi: 10.1086/307862.

J. Dyks and M. Pierbattista. The ratio of profile peak separations as a probe of pulsar radio-beam structure. MNRAS, 454:2216–2227, December 2015. doi: 10.1093/mnras/stv2118.

J. Dyks and B. Rudak. The origin of the frequency-dependent behaviour of pulsar radio profiles. MNRAS, 446:2505–2522, January 2015. doi: 10.1093/mnras/stu2262.

R. T. Gangadhara. Window-threshold technique for detecting pulse components Pages 297-298. *Bulletin of the Astronomical Society of India*, 28: 297–298, June 2000.

M. Geyer, A. Karastergiou, V. I. Kondratiev, K. Zagkouris, M. Kramer, B. W. Stappers, J.-M. Grießmeier, J. W. T. Hessels, D. Michilli, M. Pilia, and C. Sobey. Scattering analysis of LOFAR pulsar observations. MNRAS, 470:2659–2679, September 2017. doi: 10.1093/mnras/stx1151.

J. Gil, P. Gronkowski, and W. Rudnicki. Geometry of the emission region of PSR 0950+08. A&A, 132:312–316, March 1984.

P. Goldreich and W. H. Julian. Pulsar Electrodynamics. ApJ, 157:869, August 1969. doi: 10.1086/150119.

T. E. Hassall, B. W. Stappers, J. W. T. Hessels, M. Kramer, A. Alexov, K. Anderson, T. Coenen, A. Karastergiou, E. F. Keane, V. I. Kondratiev, K. Lazaridis, J. van Leeuwen, A. Noutsos, M. Serylak, C. Sobey, J. P. W. Verbiest, P. Weltevrede, K. Zagkouris, R. Fender, R. A. M. J. Wijers, L. Bähren, M. E. Bell, J. W. Broderick, S. Corbel, E. J. Daw, V. S. Dhillon, J. Eislöffel, H. Falcke, J.-M. Grießmeier, P. Jonker, C. Law, S. Markoff, J. C. A. Miller-Jones, R. Osten, E. Rol, A. M. M. Scaife, B. Scheers, P. Schellart, H. Spreeuw, J. Swinbank, S. ter Veen, M. W. Wise, R. Wijnands, O. Wucknitz, P. Zarka, A. Asgekar, M. R. Bell, M. J. Bentum, G. Bernardi, P. Best, A. Bonafede, A. J. Boonstra, M. Brentjens, W. N. Brouw, M. Brüggen, H. R. Butcher, B. Ciardi, M. A. Garrett, M. Gerbers, A. W. Gunst, M. P. van Haarlem, G. Heald, M. Hoeft, H. Holties, A. de Jong, L. V. E. Koopmans, M. Kuniyoshi, G. Kuper, G. M. Loose, P. Maat, J. Masters, J. P. McKean, H. Meulman, M. Mevius, H. Munk, J. E. Noordam, E. Orrú, H. Paas, M. Pandey-Pommier, V. N. Pandey, R. Pizzo, A. Polatidis, W. Reich, H. Röttgering, J. Sluman, M. Steinmetz, C. G. M.

Sterks, M. Tagger, Y. Tang, C. Tasse, R. Vermeulen, R. J. van Weeren, S. J. Wijnholds, and S. Yatawatta. Wide-band simultaneous observations of pulsars: disentangling dispersion measure and profile variations. A&A, 543:A66, July 2012. doi: 10.1051/0004-6361/201218970.

T. E. Hassall, B. W. Stappers, P. Weltevrede, J. W. T. Hessels, A. Alexov, T. Coenen, A. Karastergiou, M. Kramer, E. F. Keane, V. I. Kondratiev, J. van Leeuwen, A. Noutsos, M. Pilia, M. Serylak, C. Sobey, K. Zagkouris, R. Fender, M. E. Bell, J. Broderick, J. Eislöffel, H. Falcke, J.-M. Grießmeier, M. Kuniyoshi, J. C. A. Miller-Jones, M. W. Wise, O. Wucknitz, P. Zarka, A. Asgekar, F. Batejat, M. J. Bentum, G. Bernardi, P. Best, A. Bonafede, F. Breitling, M. Brüggen, H. R. Butcher, B. Ciardi, F. de Gasperin, J.-P. de Reijer, S. Duscha, R. A. Fallows, C. Ferrari, W. Frieswijk, M. A. Garrett, A. W. Gunst, G. Heald, M. Hoeft, E. Juette, P. Maat, J. P. McKean, M. J. Norden, M. Pandey-Pommier, R. Pizzo, A. G. Polatidis, W. Reich, H. Röttgering, J. Sluman, Y. Tang, C. Tasse, R. Vermeulen, R. J. van Weeren, S. J. Wijnholds, and S. Yatawatta. Differential frequency-dependent delay from the pulsar magnetosphere. A&A, 552:A61, April 2013. doi: 10.1051/0004-6361/201220764.

A. Hewish, S. J. Bell, J. D. H. Pilkington, P. F. Scott, and R. A. Collins. Observation of a Rapidly Pulsating Radio Source (Reprinted from Nature, February 24, 1968). Nature, 224:472, November 1969. doi: 10.1038/224472b0.

S. Johnston and J. M. Weisberg. Profile morphology and polarization of

young pulsars. MNRAS, 368:1856–1870, June 2006. doi: 10.1111/j.1365-2966.2006.10263.x.

P. B. Jones. Radio-frequency microstructure and polarization in ion-proton pulsars. MNRAS, 468:3878–3882, July 2017. doi: 10.1093/mnras/stx731.

A. Karastergiou and S. Johnston. An empirical model for the beams of radio pulsars. MNRAS, 380:1678–1684, October 2007. doi: 10.1111/j.1365-2966.2007.12237.x.

R. Karuppusamy, B. W. Stappers, and M. Serylak. A low frequency study of PSRs B1133+16, B1112+50, and B0031-07. A&A, 525:A55, January 2011. doi: 10.1051/0004-6361/201014507.

A. D. Kuzmin and B. Y. Losovsky. Unusual frequency dependence of the integrated profile of the millisecond pulsar PSR J2145-0705. A&A, 308:91–96, April 1996.

K. Liu, G. Desvignes, I. Cognard, B. W. Stappers, J. P. W. Verbiest, K. J. Lee, D. J. Champion, M. Kramer, P. C. C. Freire, and R. Karuppusamy. Measuring pulse times of arrival from broadband pulsar observations. *mnras*, 443:3752–3760, October 2014. doi: 10.1093/mnras/stu1420.

O. Löhmer, D. Mitra, Y. Gupta, M. Kramer, and A. Ahuja. The frequency evolution of interstellar pulse broadening from radio pulsars. 425:569–575, October 2004. doi: 10.1051/0004-6361:20035881.

Duncan Ross Lorimer and Michael Kramer. *Handbook of pulsar astronomy*, volume 4. Cambridge University Press, 2005.

A. G. Lyne and R. N. Manchester. The shape of pulsar radio beams. MNRAS, 234:477–508, October 1988. doi: 10.1093/mnras/234.3.477.

R. N. Manchester. Detection of Gravitational Waves using Pulsar Timing. *ArXiv e-prints*, April 2010.

R. N. Manchester, G. B. Hobbs, A. Teoh, and M. Hobbs. VizieR Online Data Catalog: ATNF Pulsar Catalog (Manchester+, 2005). *VizieR Online Data Catalog*, 7245, August 2005.

D. B. Melrose. Coherent Emission Mechanisms in Astrophysical Plasmas. *ArXiv e-prints*, July 2017.

F. C. Michel. A pulsar emission model - Observational tests. ApJ, 322: 822–830, November 1987. doi: 10.1086/165775.

J. A. Phillips. Radio emission altitudes in the pulsar magnetosphere. ApJ, 385:282–287, January 1992. doi: 10.1086/170936.

J. M. Rankin. Toward an empirical theory of pulsar emission. I Morphological taxonomy. ApJ, 274:333–368, November 1983. doi: 10.1086/161450.

S. M. Ransom, I. H. Stairs, A. M. Archibald, J. W. T. Hessels, D. L. Kaplan, M. H. van Kerkwijk, J. Boyles, A. T. Deller, S. Chatterjee, A. Schechtman-Rook, A. Berndsen, R. S. Lynch, D. R. Lorimer, C. Karako-Argaman, V. M. Kaspi, V. I. Kondratiev, M. A. McLaughlin, J. van Leeuwen, R. Rosen, M. S. E. Roberts, and K. Stovall. A millisecond pulsar in a stellar triple system. Nature, 505:520–524, January 2014. doi: 10.1038/nature12917.

L. Saha and J. Dyks. The fan beam model for the pulse evolution of PSR J0737-3039B. MNRAS, January 2017. doi: 10.1093/mnras/stx204.

S. E. Thorsett. Frequency dependence of pulsar integrated profiles. ApJ, 377:263–267, August 1991. doi: 10.1086/170355.

S. E. Thorsett, Z. Arzoumanian, and J. H. Taylor. PSR B1620-26 - A binary radio pulsar with a planetary companion? ApJ, 412:L33–L36, July 1993. doi: 10.1086/186933.

H. G. Wang, F. P. Pi, X. P. Zheng, C. L. Deng, S. Q. Wen, F. Ye, K. Y. Guan, Y. Liu, and L. Q. Xu. A Fan Beam Model for Radio Pulsars. I. Observational Evidence. ApJ, 789:73, July 2014. doi: 10.1088/0004-637X/789/1/73.

I. P. Williamson. Pulse broadening due to multiple scattering in the interstellar medium. 157:55, 1972.

M. Xue, N. D. R. Bhat, S. E. Tremblay, S. M. Ord, C. Sobey, N. A. Swainston, D. L. Kaplan, S. Johnston, B. W. Meyers, and S. J. McSweeney. A Census of Southern Pulsars at 185 MHz. PASA, 34:e070, December 2017. doi: 10.1017/pasa.2017.66.